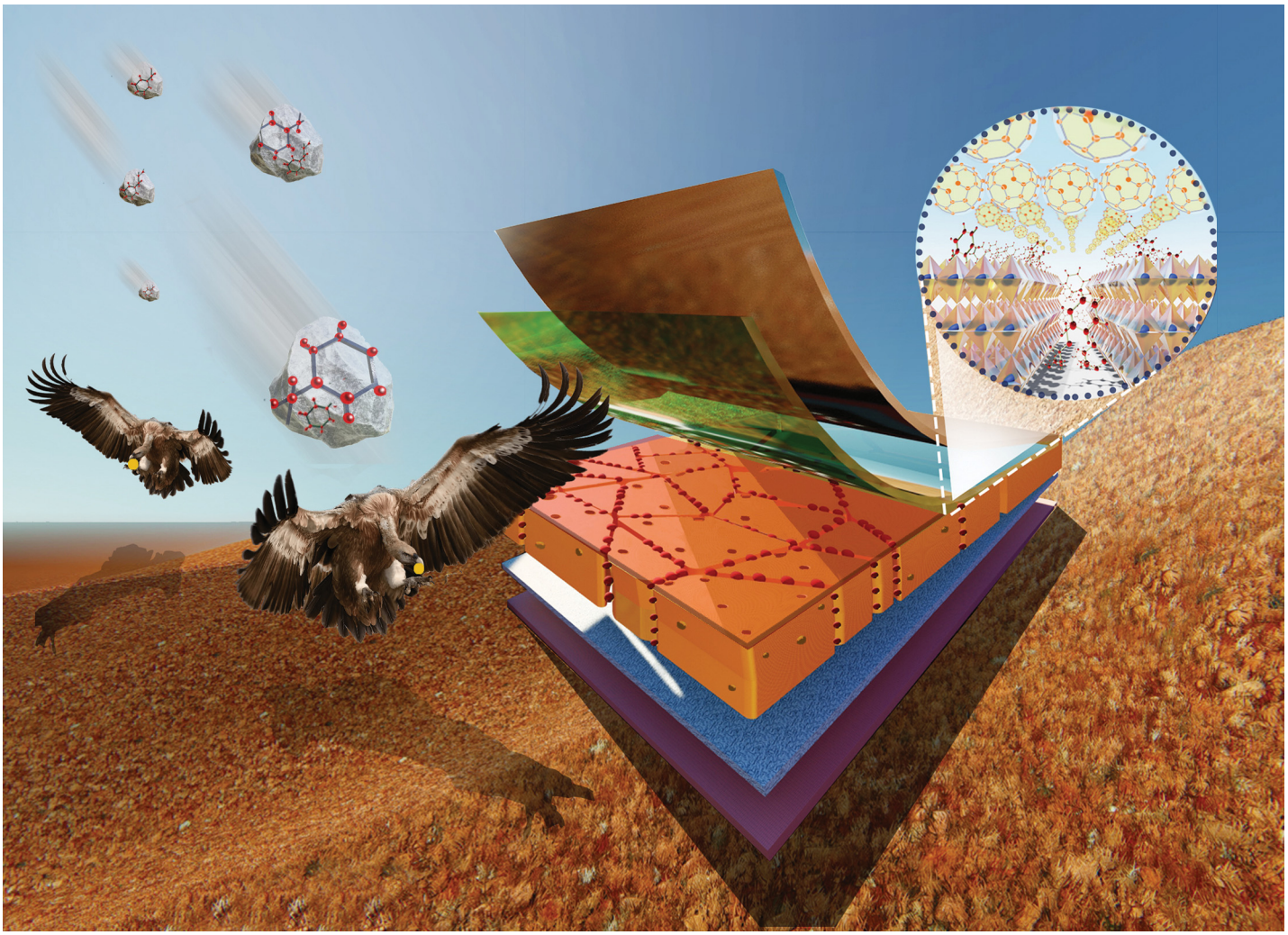

Showcasing research of Ulrich Paetzold's laboratory, Institute of Microstructure Technology & Light Technology Institute, Karlsruhe Institute of Technology, Germany.

Two birds with one stone: dual grain-boundary and interface passivation enables >22% efficient inverted methylammonium-free perovskite solar cells

Perovskite solar cells in p-i-n architecture have demonstrated great potential for flexible and perovskite-based tandem photovoltaics. This study introduces a dual passivation strategy using the long chain alkylammonium salt phenethylammonium chloride both as an additive and for surface treatment to simultaneously passivate the grain boundaries and the interface. We achieve one of the highest efficiencies for p-i-n perovskite solar cells by advancing simultaneously the open-circuit voltage and the fill factor. The presented dual passivation strategy highlights the importance of advanced defect management of the perovskite absorber layer to achieve highest performance.

As featured in:

See Ulrich W. Paetzold *et al.*, *Energy Environ. Sci.*, 2021, **14**, 5875.

ROYAL SOCIETY OF CHEMISTRY

rsc.li/ees

Registered charity number: 207890

Energy & Environmental Science

ROYAL SOCIETY OF CHEMISTRY

PAPER

View Article Online
View Journal | View Issue

Cite this: *Energy Environ. Sci.*, 2021, **14**, 5875

Two birds with one stone: dual grain-boundary and interface passivation enables >22% efficient inverted methylammonium-free perovskite solar cells†

Saba Gharibzadeh, ‡[ab] Paul Fassl, ‡[ab] Ihteaz M. Hossain,[ab] Pascal Rohrbeck,[c] Markus Frericks,[de] Moritz Schmidt,[abf] The Duong,[g] Motiur Rahman Khan,[a] Tobias Abzieher,[a] Bahram Abdollahi Nejand,[ab] Fabian Schackmar,[ab] Osbel Almora,[h] Thomas Feeney,[a] Roja Singh,[ab] Dirk Fuchs,[i] Uli Lemmer,[a] Jan P. Hofmann,[de] Stefan A. L. Weber[c] and Ulrich W. Paetzold *[ab]

Advancing inverted (p–i–n) perovskite solar cells (PSCs) is key to further enhance the power conversion efficiency (PCE) and stability of flexible and perovskite-based tandem photovoltaics. Yet, the presence of defects at grain boundaries and in particular interfacial recombination at the perovskite/electron transporting layer interface induce severe non-radiative recombination losses, limiting the open-circuit voltage (V_{OC}) and fill factor (FF) of PSCs in this architecture. In this work, we introduce a dual passivation strategy using the long chain alkylammonium salt phenethylammonium chloride (PEACl) both as an additive and for surface treatment to simultaneously passivate the grain boundaries and the perovskite/C_{60} interface. Using [2-(9*H*-carbazol-9-yl)ethyl]phosphonic acid (2PACz) as a hole transporting layer and a methylammonium (MA)-free $Cs_{0.18}FA_{0.82}PbI_3$ perovskite absorber with a bandgap of ~1.57 eV, prolonged charge carrier lifetime and an on average 63 meV enhanced internal quasi-Fermi level splitting are achieved upon dual passivation compared to reference p–i–n PSCs. Thereby, we achieve one of the highest PCEs for p–i–n PSCs of 22.7% (stabilized at 22.3%) by advancing simultaneously the V_{OC} and FF up to 1.162 V and 83.2%, respectively. Using a variety of experimental techniques, we attribute the positive effects to the formation of a heterogeneous 2D Ruddlesden–Popper $(PEA)_2(Cs_{1-x}FA_x)_{n-1}Pb_n(I_{1-y}Cl_y)_{3n+1}$ phase at the grain boundaries and surface of the perovskite films. At the same time, the activation energy for ion migration is significantly increased, resulting in enhanced stability of the PSCs under light, humidity, and thermal stress. The presented dual passivation strategy highlights the importance of defect management both in the grain boundaries and the surface of the perovskite absorber layer using a proper passivation material to achieve both highly efficient and stable inverted p–i–n PSCs.

Received 18th May 2021,
Accepted 3rd August 2021

DOI: 10.1039/d1ee01508g

rsc.li/ees

[a] *Light Technology Institute, Karlsruhe Institute of Technology, Engesserstrasse 13, 76131 Karlsruhe, Germany. E-mail: ulrich.paetzold@kit.edu*
[b] *Institute of Microstructure Technology, Karlsruhe Institute of Technology, Hermann-von Helmholtz-Platz 1, 76344 Eggenstein-Leopoldshafen, Germany*
[c] *Max Planck Institute for polymer research, department physics at interfaces, Ackermannweg 10, 55128 Mainz, Germany*
[d] *Technical University of Darmstadt, Department of Materials and Earth Sciences, Surface Science Laboratory, Otto-Berndt-Strasse 3, 64287 Darmstadt, Germany*
[e] *InnovationLab GmbH, Speyerer Strasse 4, 69115 Heidelberg, Germany*
[f] *Center for Nanophotonics, AMOLF, 1098 XG Amsterdam, The Netherlands*
[g] *School of Engineering, The Australian National University, Canberra, 2601, Australia*
[h] *Institute of Advanced Materials, Universitat Jaume I, 12006 Castelló, Spain*
[i] *Insitute for Quantum Materials and Technologies, Karlsruhe Institute of Technology, Herrmann-von-Helmholtz-Platz 1, 76344 Eggenstein-Leopoldshafen, Germany*

† Electronic supplementary information (ESI) available. See DOI: 10.1039/d1ee01508g

‡ These authors contributed equally to this work.

Broader context

Due to the rapid increase in power conversion efficiency of perovskite solar cells (PSCs), they are considered an emerging area of research in photovoltaic technologies. While inverted p–i–n PSCs have demonstrated great potential for flexible and perovskite-based tandem photovoltaics, key challenges still need to be addressed as compared to their n–i–p counterparts. In particular, severe non-radiative recombination losses induced by the presence of defects at grain boundaries (GBs) and interfacial recombination at the perovskite/electron transporting layer interface limit the open-circuit voltage (V_{OC}) and fill factor (FF) of PSCs in this architecture. To address this issue, we demonstrate that utilizing a dual passivation strategy using phenethylammonium chloride both as an additive and for surface treatment simultaneously passivates defects at the GBs and the perovskite/C_{60} interface. We show that this is due to the formation of a heterogeneous 2D Ruddlesden-Popper phase, leading to a significant improvement in both the V_{OC} and FF. In view of the urge to advance p–i–n PSCs for flexible and perovskite-based tandem photovoltaics, our findings stress the importance of defect management both at the GBs and the surface of the perovskite absorber layer in order to achieve both highly efficient and stable inverted p–i–n PSCs.

Introduction

Single-junction organic–inorganic metal halide perovskite solar cells (PSCs) have demonstrated outstanding performance in laboratory-scale devices, closing the gap to the highest reported power conversion efficiencies (PCEs) of the market-dominating Si solar cells.[1,2] While PCEs above 23% have been demonstrated using the mesoporous[3–12] and planar[13–22] n–i–p architecture (up to 25.5% certified[23]), inverted planar p–i–n PSCs still lag behind despite several recent studies reporting PCEs above 22% (up to 22.75% certified[24]) (see Fig. S1, ESI†).[20,24–30] Further increasing the PCE of p–i–n PSCs is crucial given (1) their compatibility with p-type Si bottom solar cells for monolithic perovskite/Si tandem photovoltaics (PV),[31,32] (2) their low-temperature processability ($\leq$100 °C), and (3) their promising operational stability along with negligible hysteresis.[33]

The most relevant bottleneck limiting the PCE of p–i–n PSCs is the apparent non-radiative recombination losses at the interface between the perovskite and the charge transport layers (CTLs).[33–39] As a result, the open-circuit voltage (V_{OC}) of p–i–n PSCs relative to the Shockley–Queisser (S–Q) limit for a given bandgap has long been significantly lower as compared to their n–i–p counterparts (Fig. S2a, ESI†), while recently specifically the V_{OC} × fill factor (FF) product is lagging behind (Fig. S2b, ESI†).[31,33,34] Considering that the novel self-assembled monolayer (SAM) hole transport layers (HTLs) 2PACz ([2-(9*H*-carbazol-9-yl)ethyl]phosphonic acid) and Me-4PACz ([2-(3,6-dimethoxy-9*H*-carbazol-9-yl)ethyl]phosphonic acid) developed by Albrecht and coworkers form a practically lossless interface,[31,32] the remaining challenge is interfacial recombination at the electron transport layer (ETL), which is commonly the fullerene C_{60} or phenyl-C_{61}-butyric acid methyl ester (PCBM). The second most relevant bottleneck is bulk defects in conjunction with the abundance of grain boundaries in perovskite films. Although the electronic properties of grain boundaries are still debated,[40–42] they are commonly associated with an increased defect density, facilitated ion migration and an accelerated degradation under light and thermal stress.[43–47] The latter aspect is particularly important considering that stability is one of the main concerns for the future commercialization of perovskite PVs.[48–51] For these reasons, effective strategies to reduce both, (1) interfacial recombination at surface/interface defects and (2) bulk recombination at bulk or grain boundary defects are pivotal to maximize both the V_{OC} and FF as well as the stability of planar p–i–n PSCs.

Post-treatment of perovskite films is a widely established strategy to suppress interfacial recombination and optimize the performance of PSCs.[49,52–58] Prominent examples for tailored passivation schemes are the use of (alkyl)ammonium salts,[3,4,6,10,11,13,14,20,22,59–80] other organic compounds[16,19,24,45,81–87] and fluoride-containing materials.[31,35,38,74,86,88,89] Alongside established chemical passivation that reduces the density of surface/interface defects,[53,63,83,85] this strategy also encompasses performance enhancements by the formation of 2D/3D heterostructures[10,59–61,63,64,70,76–78] and/or wide-bandgap interface layers.[6,66,90,91] The latter enhancements can be the result of improved energy level alignment that promotes selectivity and carrier transport across perovskite/CTL interfaces and/or a reduced probability for interfacial recombination due to charge blocking.[19,25,35,53,67,77,92] Recently, lithium fluoride (LiF) has been identified as an interlayer at the perovskite/ETL interface that significantly enhances the performance of p–i–n PSCs.[31,35,38,88,89,93] However, PSCs with LiF undergo severe long-term degradation which limits the applicability of this approach.[31,93]

In order to reduce non-radiative recombination in the bulk and grain boundaries, the use of non-stoichiometric precursors[94–96] or incorporation of different additives into the perovskite precursor solution or antisolvent such as metal cations,[97] anions,[98] chloride (Cl) or thiocyanate (SCN),[4–6,10,14,15,17,19,88] (alkyl)ammonium salts,[3,25,26,64,98–105] other organic compounds,[74,84,106] and fluoride-containing materials[74,107] have been proposed. Given that these additives directly assist in perovskite film formation, changes in crystallization dynamics as well as a reduced defect density are commonly observed.[55,108,109] For instance, Xu *et al.* demonstrated that by alloying $MAPbCl_3$ into the perovskite film, the V_{OC} of the wide-bandgap p–i–n PSCs significantly improved due to a reduced bulk defect density.[88] In other works, the addition of various long chain alkylammonium cations was shown to self-assemble into a wide-bandgap 2D perovskite phase passivating the surface and/or grain boundaries of the 3D perovskite film.[25,58,64,99–105] However, due to the insulating nature of such 2D phases, adding too large amounts typically results in an overall lower PCE compared to control devices.[25,64,99,101,103,104,107]

Despite the apparent wide range of strategies suggested to reduce non-radiative recombination losses in PSCs,[49,54,57,110,111]

to our knowledge there is only one recent report that used the same passivation material both as an additive and for surface treatment to improve the performance of p–i–n PSCs.[84] In this work, we report on an effective dual passivation approach using the long chain alkylammonium salt phenethylammonium chloride (PEACl) to simultaneously passivate the grain boundaries and the perovskite/C_{60} interface by using PEACl:$PbCl_2$ as the additive and PEACl for surface treatment, respectively. Employing time-resolved photoluminescence (TRPL) and photoluminescence quantum yield (PLQY) measurements, dual passivation is proven to be most effective in reducing non-radiative recombination compared to either of the individual passivation strategies. By analyzing cathodoluminescence (CL), scanning electron microscopy (SEM), X-ray/ultraviolet photoelectron spectroscopy (XPS/UPS), X-ray diffraction (XRD) and Kelvin probe force microscopy (KPFM) measurements, we attribute the positive effects to the formation of a heterogeneous 2D Ruddlesden–Popper (RP) $(PEA)_2(Cs_{1-x}FA_x)_{n-1}Pb_n(I_{1-y}Cl_y)_{3n+1}$ perovskite phase with $n \sim 1$–2 at the surface and grain boundaries of the film that exhibits a lower work function (WF) and hole blocking properties. Finally, thermal admittance spectroscopy (TAS) reveals that the activation energy for ion migration is strongly increased upon dual passivation, which is reflected in an enhanced device stability under maximum power point (MPP) tracking and heat treatment for 1000 h. In summary, by using PEACl both as the additive and for surface treatment, we could not only effectively reduce interfacial recombination at the perovskite/C_{60} interface, but simultaneously passivate the grain boundary defects. Employing dual passivation for methylammonium (MA)-free p–i–n PSCs with a bandgap of ~1.57 eV leads to a very high PCE of 22.7% (stabilized at 22.3%) with a remarkable V_{OC} and FF of up to 1.162 V and 83.2%, respectively. In view of the urge to advance the p–i–n structure for flexible and perovskite-based tandem photovoltaics, this development is pivotal.

Results and discussion

The dual passivation strategy developed in this work is based on combining the incorporation of PEACl:$PbCl_2$ into the perovskite precursor solution and PEACl surface treatment (Fig. 1). Since using long chain alkylammonium salts as additive mainly passivates the grain boundaries, as will be shown later and has been proposed in previous works,[26,98,101–103] it is for simplicity referred to as grain boundary passivation (GBP) in the following, while surface treatment is referred to as surface passivation (SP). For the reference perovskite films (referred to as Ref), we adapt an established fabrication route,[112] yielding high-quality MA-free films with a composition of $Cs_{0.18}FA_{0.82}PbI_3$ (10% excess PbI_2) and a bandgap of ~1.57 eV. In case of GBP, PEACl : $PbCl_2$ (1 : 1 molar ratio) dissolved in dimethyl sulfoxide (DMSO) is added into the Ref precursor solution (optimized at a concentration of 2 mol%; see Fig. S3, ESI†). The Ref and GBP precursor solutions are spin-coated on top of ITO/2PACz and annealed at 150 °C for 30 min (Fig. 1a). In case of SP, PEACl dissolved in isopropanol (optimized at a concentration of 1.5 mg ml^{-1}; see Fig. S4, ESI†), is dynamically spin-coated on the surface of $Cs_{0.18}FA_{0.82}PbI_3$

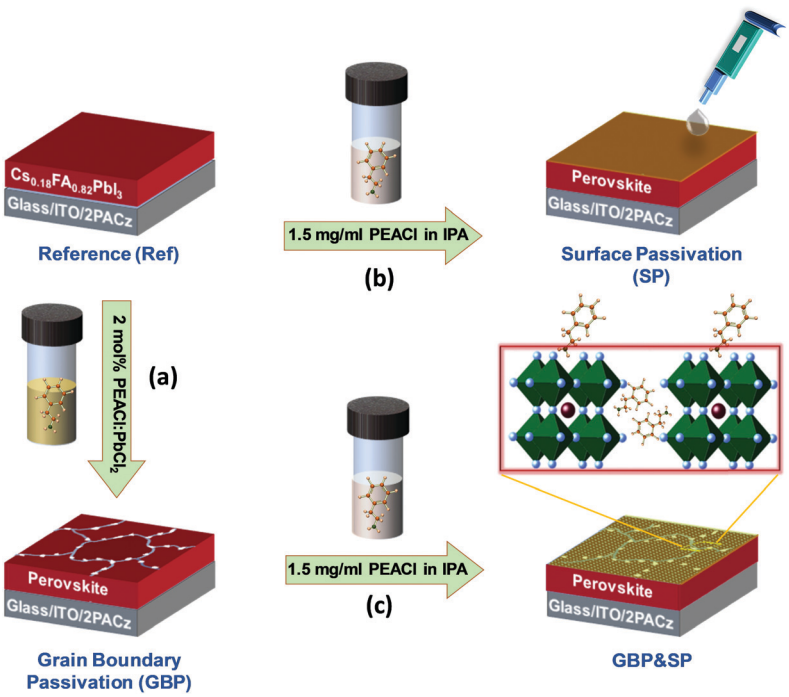

Fig. 1 Schematic of the perovskite absorber deposition process employing the dual passivation strategy developed in this work: (a) grain boundary passivation (GBP) by incorporation of PEACl:$PbCl_2$ into the perovskite precursor solution, (b) surface passivation (SP) by treatment of PEACl in IPA on top of the perovskite absorber layer and (c) combination of grain boundary and surface passivation (GBP&SP).

films and subsequently annealed at 100 °C for 10 min (Fig. 1b). Finally, both individual passivation strategies are exploited together, referred to as GBP&SP (Fig. 1c). Further details are provided in the Experimental Section (ESI†).

Photovoltaic performance

In order to demonstrate the trend in performance of planar p–i–n PSCs upon employing either individual passivation (GBP or SP) as well as dual passivation (GBP&SP) compared to Ref PSCs, devices in the layer stack ITO/2PACz/perovskite/C_{60}/BCP/Ag with an active area of 12.3 mm^2 were prepared (Fig. 2a). Fig. 2b and Table S1 (ESI†) summarize the current density–voltage (*J*–*V*) characteristics and PV parameters of the best-performing p–i–n PSCs. The corresponding statistics (in total 147 devices) that emphasize the very high yield and good reproducibility of the key trends are shown in Fig. 2c. The best Ref PSC exhibits a PCE of 20.4% with a short-circuit current density (J_{SC}) of 23.9 mA cm^{-2}, a V_{OC} of 1.086 V, and a FF of 78.6%. This denotes a very respectable starting point in performance for p–i–n PSCs compared to literature (see Fig. S1, ESI†). The PCE of the best GBP PSC is slightly improved to 20.7%, which is mainly associated with a 26 mV enhancement in V_{OC} as well as a slightly improved FF. The small decrease in J_{SC} to 23.6 mA cm^{-2} is attributed to the formation of a 2D RP perovskite (see discussion in the following) and, thus, a slight decrease in 3D perovskite absorber volume (see ultraviolet-visible (UV-vis) measurements in Fig. S5, ESI†).[64,99] The best SP PSC already exhibits a very high PCE of 22.1% with a significant improvement in both the V_{OC} (1.131 V) and FF (82.3%) as compared to the Ref PSC.

Strikingly, upon dual passivation, the V_{OC} and FF are further enhanced to 1.162 V and 83.2% respectively, which leads to a remarkable PCE of 22.7% for the best GBP&SP PSC (see Fig. 2d). This corresponds to a V_{OC} × FF product of 0.891 with respect to the S–Q limit, the highest reported for p–i–n PSCs with a PCE above 21% (compare Fig. S1 and S2b, ESI†). Furthermore, the GBP&SP PSC also exhibits a remarkable stabilized PCE (under MPP tracking), V_{OC} and J_{SC} of 22.3%, 1.161 V and 23.4 mA cm^{-2} under continuous AM1.5G illumination for 5 min, respectively (Fig. 2e). It should be noted that the V_{OC} enhancements are not governed by an increase in the bandgap, as shown by analysis *via* the Tauc plot method and the inflection point of the EQE spectra (Fig. S6a and b, ESI†),[113] but relate to reduced non-radiative recombination, as we will later elaborate on in detail. We note that when increasing the concentration of PEACl to 3 mg ml^{-1} (beyond the optimum concentration), the V_{OC} of GBP&SP PSCs increases further up to 1.184 V (see Fig. S4, ESI†), which represents a voltage deficit of only 393 mV and 104 mV with respect to the bandgap and radiative limit respectively (90.9% of the S–Q limit),[113] that are among the lowest reported for p–i–n PSCs (Fig. S2a, ESI†). However, since the J_{SC} and FF decline at the same time, possibly due to the insulating nature of a thicker 2D RP passivation layer at the surface,[63,64,81,82,99] the PCE of the best GBP&SP PSC drops to 21.8%. It should be noted that the reported J_{SC} for all PSCs is corrected using the ratio of J_{SC} derived from the external quantum efficiency (EQE) and *J*–*V* measurements of the best PSCs (Fig. 2b and Fig. S7, ESI†).

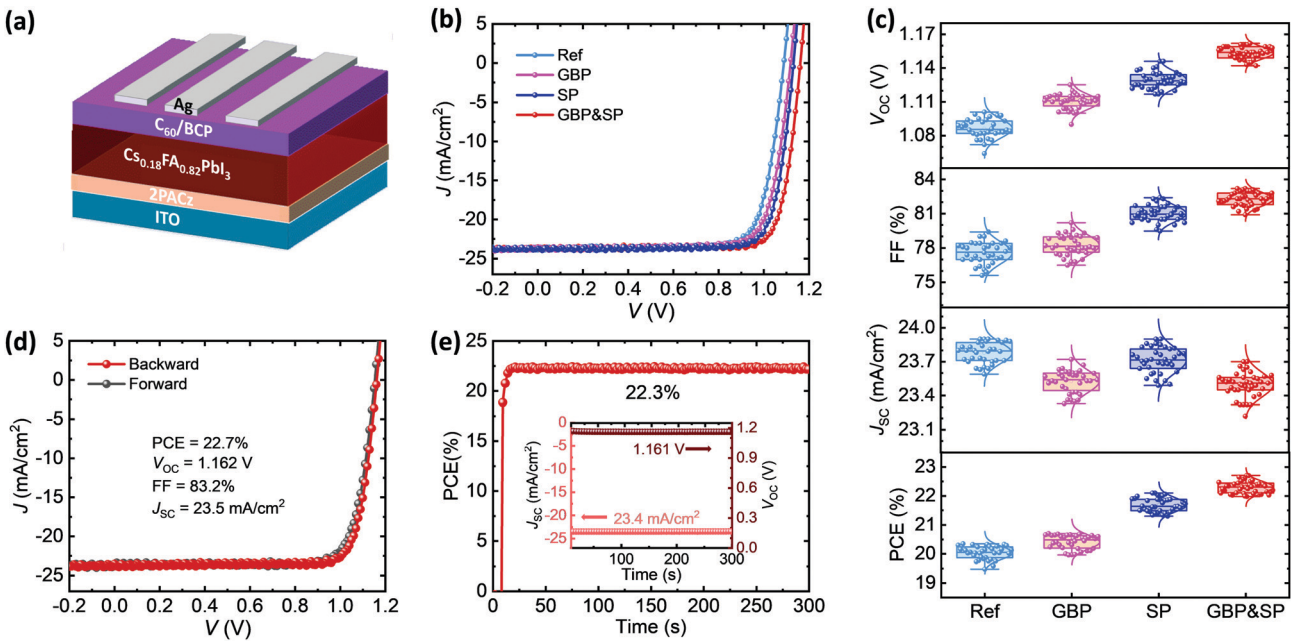

Fig. 2 (a) Schematic of the employed perovskite solar cell configuration with a layer stack sequence of ITO/2PACz/perovskite/C_{60}/BCP/Ag. (b) Current density *versus* voltage (*J*–*V*) characteristics and (c) statistical distribution of the open-circuit voltage (V_{OC}), fill factor (FF), short-circuit current density (J_{SC}), and power conversion efficiency (PCE) of perovskite solar cells without any modification (Ref), with surface passivation (SP), grain boundary passivation (GBP) and combined grain boundary and surface passivation (GBP&SP). (d) *J*–*V* characteristics and (e) maximum power point (MPP) tracking of the best-performing GBP&SP perovskite solar cell, demonstrating a stabilized PCE of 22.3%. The inset shows the stabilized J_{SC} and V_{OC}.

This results in a rather conservative determination of PCE in this work. To summarize, the combined enhancements in V_{OC} and FF are highest for GBP&SP PSCs, which highlights the necessity of the simultaneous passivation of the perovskite/C_{60} interface, and – as we will show later – the grain boundaries of the perovskite thin film.

Next to dual passivation by PEACl, we first evaluated the effect on the V_{OC} upon employing PEAI and PEABr, since they have been used in numerous previous reports for passivation of perovskite films.[62,65,69,77,99,103] As shown in Fig. S8 (ESI†), PEACl-based GBP&SP PSCs show a much higher average of V_{OC} of ~1.15 V as compared to ~1.12 V in case of PEAI and PEABr. Therefore, we focussed in more detail on alternative chloride-based long chain alkylammonium salts namely *n*-butylammonium chloride (BACl) and *n*-octylammonium chloride (OACl), since BAI,[63,64,71,72,76,102] BABr,[10,59,60,64] OAI,[4,72,75,76,101] and OABr[10,71] have previously been reported to serve as efficient passivation molecules as additive as well as for surface treatment.

While SP PSCs all exhibit an enhanced V_{OC} and FF as compared to Ref PSCs, the enhancements are most pronounced in case of PEACl (Fig. S9, ESI†). Employing the dual passivation strategy leads to a ~30 mV V_{OC} enhancement in case of OACl and BACl, which is much lower compared to ~70 mV for PEACl-based GBP&SP PSCs (see Fig. S10, ESI†). Furthermore, while for BACl-based GBP&SP PSCs the FF remains similar and only a slight drop in J_{SC} is observed compared to Ref PSCs, these parameters are even reduced in case of OACl, as expected based on previous reports employing too large amounts of alkylammonium salts as additive.[25,64,99,102] Therefore, an overall lower average PCE of only 18.6% is obtained for OACl-based GBP&SP PSCs compared to 20.1% for Ref PSCs, while the average PCE is slightly higher at 20.9% in case of BACl. These results highlight that our dual GBP&SP passivation strategy in principle is compatible with other Cl-based long chain alkylammonium salts, but reduced charge carrier transport (*i.e.*, lower J_{SC} and/or FF) can easily impede any positive effects from reduced interfacial recombination (*i.e.*, higher V_{OC}). Hence, careful optimization of the fabrication parameters is required. Targeting high efficiency and reproducibility, we identified PEACl as the superior choice for the dual passivation strategy of p–i–n PSCs studied in this work.

Photophysical properties

To discriminate the effect of GBP, SP and GBP&SP on non-radiative recombination of the PSCs, we first show representative TRPL transients measured for ITO/2PACz/perovskite/C_{60} layer stacks in Fig. 3a. While the detailed interpretation of such transients can be challenging,[114] a longer monomolecular

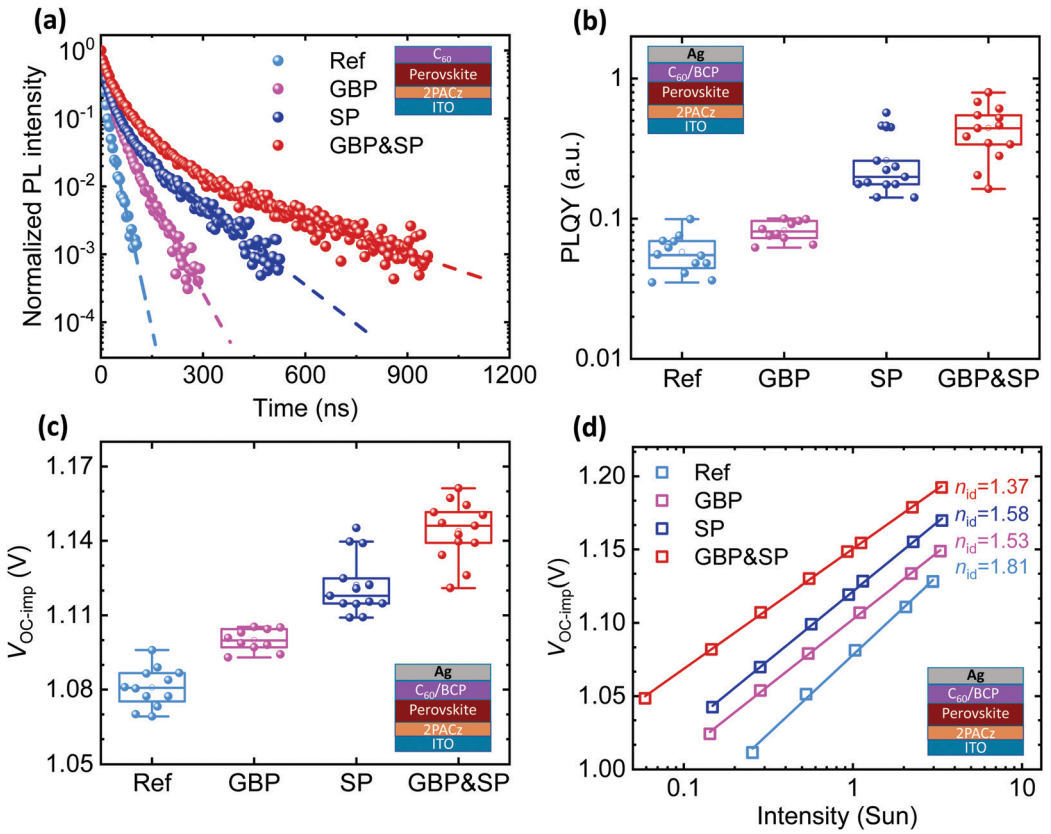

Fig. 3 (a) Time-resolved photoluminescence (TRPL), (b) photoluminescence quantum yield (PLQY), (c) the obtained implied V_{OC} ($V_{OC\text{-}imp}$), and (d) ideality factor (n_{id}) extracted from a fit to the intensity-dependent $V_{OC\text{-}imp}$ of the perovskite films prepared on ITO/2PACz substrates for the reference (Ref), surface passivation (SP), grain boundary passivation (GBP) and grain boundary & surface passivation (GBP&SP) films. TRPL in (a) is measured with a C_{60} layer on top, while (b–d) are measured for a full device stack.

lifetime at low-level injection can be attributed to reduced non-radiative recombination either within the bulk (including the grain boundaries) or the perovskite/CTL interfaces.[114–117] The lifetime increases considerably by more than one order of magnitude in the order ref (19 ns) → GBP (48 ns) → SP (113 ns) → GBP&SP (256 ns) (dashed lines Fig. 3a). This indicates that non-radiative recombination is effectively suppressed in the same order as the observed V_{OC} enhancement of the PSCs.[114–117]

To quantify the reduction of non-radiative recombination, PLQY measurements along with the internal quasi-Fermi level splitting (E_F), that are attributed to the 'implied V_{OC}' *via* $V_{OC\_imp} = \Delta E_F/q = V_{OC\_rad} + k_BT/q \ln(\text{PLQY})$, are discussed next.[34,118] Analysing PLQY and V_{OC_imp} for the stack ITO/2PACz/perovskite without C_{60} allows identification of whether non-radiative recombination at the HTL/perovskite limits the V_{OC} of our PSCs.[34,35,39] For the Ref films, we find an already very high average PLQY (V_{OC_imp}) of 7.2% (1.206 V) which only slightly increases to 7.9% (1.218 V), 9.8% (1.218 V) and 9.7% (1.225 V) for GBP, SP and GBP&SP films, respectively (Fig. S11, ESI†), with V_{OC_imp} being well above the obtained V_{OC} of all PSCs presented in Fig. 2c. This shows that our perovskite films are of very high quality and that the nearly lossless 2PACz/perovskite interface does not limit the V_{OC}, in line with previous reports.[31,32,35] Upon addition of C_{60}/BCP/Ag, the PLQY for Ref films severely drops to a low average value of 0.058% correlating to V_{OC_imp} of 1.081 V, clearly showing that the perovskite/C_{60} interface limits the V_{OC} (Fig. 2b and c). Impressively, the average PLQY increases by roughly one order of magnitude to 0.083%, 0.26% and 0.45% for GBP, SP, and GBP&SP films respectively (Fig. 3b), correlating to an enhanced V_{OC_imp} of 1.100 V, 1.122 V and 1.144 V, respectively (Fig. 3c). Notably, the values of V_{OC_imp} closely match with the average V_{OC} of the respective PSCs (compare Fig. 2c), implying that all PSCs have a proper energetic alignment that does not result in an offset between V_{OC_imp} and V_{OC}.[34,35,92,118,119] We note that increasing the PEACl concentration to 3 mg ml^{-1} for GBP&SP films further increases the PLQY and V_{OC_imp} to remarkable values of up to 2.21% and 1.190 V, respectively, which is in line with the results discussed above for the respective PSCs (see Fig. S12, ESI†).

At first sight, the role of the PEACl:$PbCl_2$ additive for the improved device performance remains unclear, since V_{OC_imp} for the half layer stack without C_{60} only slightly increases for all passivation strategies as compared to Ref films. To shed more light on this aspect, we show representative TRPL transients for the stack ITO/2PACz/perovskite in Fig. S13 (ESI†). Here, we find a clear trend with the monomolecular lifetime for GBP films (~1624 ns) and GBP&SP films (~1497 ns) being considerably longer as compared to Ref films (~335 ns). Interestingly, for perovskite films with surface passivation only, the lifetime is solely slightly increased to ~464 ns. At this point, we hypothesize that the enhanced lifetimes in case of GBP relate to the passivation of shallow grain boundary traps *via* the self-assembly of PEA^+ molecules and/or the formation of a PEACl-based 2D RP phase.[25,26,36,41,46,102,104–106,120,121] We note that shallow traps are typically filled at high illumination intensities around 1 Sun, possibly explaining why the values of PLQY and V_{OC_imp} for stacks without C_{60} are only slightly enhanced by all three passivation strategies. This explanation is in line with the common implication that grain boundaries are not necessarily detrimental to device performance at solar illumination intensities.[40,41,120] To shed more light on this, we evaluate the trap-state density (n_t) and charge carrier mobility (μ) of electrons and holes for the different passivation strategies *via* space charge limited current (SCLC) measurements. We fabricated both electron- and hole-only devices with the configuration of ITO/SnO_2/perovskite/C_{60}/BCP/Ag and ITO/2PACz/perovskite/Spiro-MeOTAD/Ag, respectively. The dark *J–V* characteristics of the devices are plotted in Fig. S14 and S15 (ESI†) and are analyzed according to the SCLC method (see further details in the ESI†). The electron mobility of the Ref device is 4.9×10^{-3} cm^2 V^{-1} s^{-1}, while both SP and GBP devices demonstrate a comparable increase in mobility to 6.3×10^{-3} and 7.2×10^{-3} cm^2 V^{-1} s^{-1} (see Table S2, ESI†), respectively. Applying our dual passivation strategy, the electron mobility further increases to 10.0×10^{-3} cm^2 V^{-1} s^{-1}. Furthermore, the trap-filled limit voltage (V_{TFL}), which is linearly proportional to the trap-state density, demonstrates a substantial decrease in the order Ref → GBP → SP → GBP&SP, correlating to a reduction in electron trap density from 9.2×10^{15} cm^{-3} to 6.5×10^{15}, 5.4×10^{15} and 3.7×10^{15} cm^{-3}, respectively (see Fig. S14 and Table S2, ESI†). A very similar trend is also observed for the calculated hole mobilities, while the reduction in the hole trap density is apparently slightly less pronounced (see Fig. S15 and Table S3, ESI†). Therefore, the TRPL and SCLC results indicate that both GBP and SP independently contribute to enhancing both the electron- and hole mobilities by roughly a factor of 2, while at the same time specifically reducing the electron trap density at the grain boundaries and surface of the perovskite film.

To assess the impact of the reduced trap-state density on device performance, we perform intensity-dependent PLQY measurements to obtain the internal ideality factor (n_{id}) from a fit to the calculated V_{OC_imp}.[34] The ideality factor has been proven to be governed by bulk as well as interfacial recombination properties.[34,122,123] For high-performing PSCs that are not limited by failures at either of the perovskite/CTL interfaces, a reduction of n_{id} towards a value of 1 is typically associated with a predominant bimolecular radiative and reduced trap-assisted Shockley–Read Hall recombination and there is a direct correlation between n_{id} and FF.[31,34,122,124] Again, we first analyse half-layer stacks without C_{60} and find a considerable reduction of n_{id} from 1.71 for Ref films to 1.48 and 1.60 for GBP and SP films, respectively, while GBP&SP films show by far the lowest n_{id} of 1.30 (Fig. S16, ESI†). The observation that n_{id} in case of GBP is slightly lower as compared to SP is in line with the enhanced monomolecular lifetime for GBP films without a C_{60} layer. Yet, despite the apparently improved bulk recombination properties, GBP PSCs remain severely limited by interfacial recombination at the perovskite/C_{60} interface, as exemplified by the lower device V_{OC} and FF. Interestingly, n_{id} of complete PSC layer stacks shows a very similar trend, with Ref PSCs exhibiting n_{id} of 1.81, which considerably reduces to 1.53 and 1.58 for GBP and SP PSCs,

respectively (Fig. 3d). Critically, GBP&SP PSCs again show by far the lowest n_{id} of 1.37, only slightly higher as for the half-layer stack without C_{60}. This is among the lowest n_{id} values reported in the literature for p–i–n PSCs with a PCE > 20% and slightly below the value reported by Al Ashouri *et al.* for 2PACz-based wide-bandgap PSCs.[26,31,34,38] We note that when increasing the PEACl concentration to 3 mg ml^{-1}, n_{id} of SP and GBP&SP PSCs increases again to 1.49 and 1.42 (Fig. S17, ESI†), respectively, showing that while the V_{OC} of the respective PSCs further increases (Fig. S4, ESI†), the recombination behaviour does not further benefit from too thick passivation layers, to some extent contributing to the reduced FF.

Finally, using the ideality factor and PLQY values we can determine the implied PCE and FF without and with C_{60} and compare it with an ideal device (*i.e.*, n_{id} = 1) that has the same bandgap and J_{SC}.[34] This allows us to estimate the remaining losses in our devices, *i.e.* the FF losses due to series/shunt resistance, non-ideal n_{id} and non-radiative recombination.[34,125] As shown in Fig. S18 (ESI†), the ideal device exhibits a PCE of 27.8% with a FF of 90.3% for both Ref and GBP&SP. Without and with C_{60}, Ref (GBP&SP) exhibits an implied FF of 84.8% (87.7%) and 82.8% (86.6%), respectively, while the respective best PSCs show a FF of 78.6 (83.2%). This relates to a FF loss due to series/shunt resistance of roughly 4.2% (3.4%), while non-ideal n_{id} and non-radiative recombination account for another 2% (1.1%) from C_{60} and 5.5% (2.6%) from the bulk. This analysis reveals that, in addition to strongly enhancing the V_{OC}, our dual passivation approach (GBP&SP) reduces the FF losses by 4.6% absolute as compared to Ref PSCs due to a reduced series/shunt resistance (0.8%) as well as simultaneous passivation of the perovskite/C_{60} interface (0.9%) and grain boundaries (2.9%).

In summary, the TRPL and PLQY results show that (i) the perovskite/C_{60} interface limits the V_{OC} of our PSCs and (ii) that grain boundary passivation becomes specifically crucial in the case where the perovskite/CTL interfaces are already well passivated. Therefore, in line with the device data presented, we find that dual passivation is required to reach both the lowest non-radiative recombination losses and the lowest n_{id} that only together result in the highest V_{OC} and FF.

Material characterization

Having demonstrated that the superior performance of our dual passivation strategy stems from reduced non-radiative recombination at the grain boundaries as well as at the perovskite/C_{60} interface, the question arises: How do SP and GBP modify the perovskite film morphology, structure or composition? To start with, we examine the films by SEM and identify a similar surface morphology and grain size distribution for the Ref and SP perovskite films (see Fig. S19a and b, ESI†). This observation is in line with the literature as surface treatment with low concentration long chain alkylammonium salts commonly does not alter the perovskite film morphology; more distinct changes to the morphology are only observed for higher concentrations (see Fig. S20, ESI†).[59,60,62,64,65,90] Further analysis of atomic force microscopy (AFM) images reveals a slight reduction in the root-mean-square surface roughness, which we attribute to the fact that PEACl preferentially fills regions close to the grain boundaries (Fig. S21, ESI†).[10,14] For all perovskite films, the grains that appear brighter in SEM are attributed to PbI_2-rich crystallites as will be discussed later in more detail.[17,95]

By incorporating PEACl:$PbCl_2$ in the film for GBP films, the size of the perovskite grains remains largely unchanged, however, the number and size of the PbI_2-rich grains slightly increase (Fig. S19c, ESI†). Interestingly, notable small bright crystallites appear on the surface of the perovskite film which are specifically embedded close to the grain boundaries. This indicates that PEACl:$PbCl_2$ leads to passivation mainly near the grain boundaries. Upon additional surface treatment with PEACl for GBP&SP films, the size of these small bright crystallites is reduced and they appear more dispersed all over the surface, growing with a plate-like appearance perpendicular to the perovskite grains (Fig. S19d, ESI†). This implies that some reaction with these crystallites occurs when PEACl is deposited on top of GBP films.

To gain a better understanding about the phase or composition of the small and large bright grains observed in SEM at the surface of the perovskite films as well as their potential relevance in the context of this work, we carry out CL measurement.[126] For the Ref film, the grains which appear darker in SEM (highlighted by a green circle in Fig. 4) exhibit higher CL intensities (Fig. 4b) with the emission peak located at ~774 nm (Fig. S22, ESI†) that correlates with the 3D perovskite phase with a bandgap of ~1.57 eV (note that the CL setup is not spectrally calibrated). The grains which appear brighter and exhibit a different texture in the SEM images (highlighted by a yellow circle in Fig. 4; see further top-view SEM images in Fig. S23, ESI†) demonstrate lower CL intensities (dark spots in Fig. 4b) with a CL emission peak around 500 nm (Fig. S22, ESI†). By applying a 500 nm ± 40 nm bandpass filter to record the CL image, these grains can be clearly distinguished from the 3D perovskite grains (Fig. 4c). These regions are therefore attributed to PbI_2-rich crystallites, in line with previous reports,[17,64] and as seen from cross-sectional SEM images, they appear to be located on top of 3D perovskite grains (Fig. S24, ESI†). Looking specifically at the CL signal from individual large PbI_2-rich grains, there is indeed still a signal from the (underlying) 3D perovskite phase (Fig. S22, ESI†). For the SP film, we observe a slight charging of the SEM images (Fig. 4d), which we attribute to the insulating nature of a 2D RP phase forming at the surface. No noticeable change in the CL images of the SP film without and with 500 nm ± 40 nm bandpass filter is observed compared to the Ref film (Fig. 4e and f). This indicates that the large PbI_2-rich grains are not completely chemically reacting upon PEACl surface treatment, which is in contrast to previous observations that bright PbI_2 related grains vanish upon treatment with various organic halides.[11,20,66,77,78,84] Nevertheless, due to the passivation effect, the CL signal of the 3D perovskite phase exhibits a much higher intensity compared to the Ref film (Fig. S25, ESI†), in line with the PLQY results. For the GBP film, the grains which appear as small bright grains close to the grain boundaries in SEM (highlighted by a red circle in Fig. 4g) are detected as dark small spots around the perovskite grains in the CL image (Fig. 4h). This stresses that these small grains exhibit lower CL intensities similar to the large PbI_2-rich grains. Interestingly,

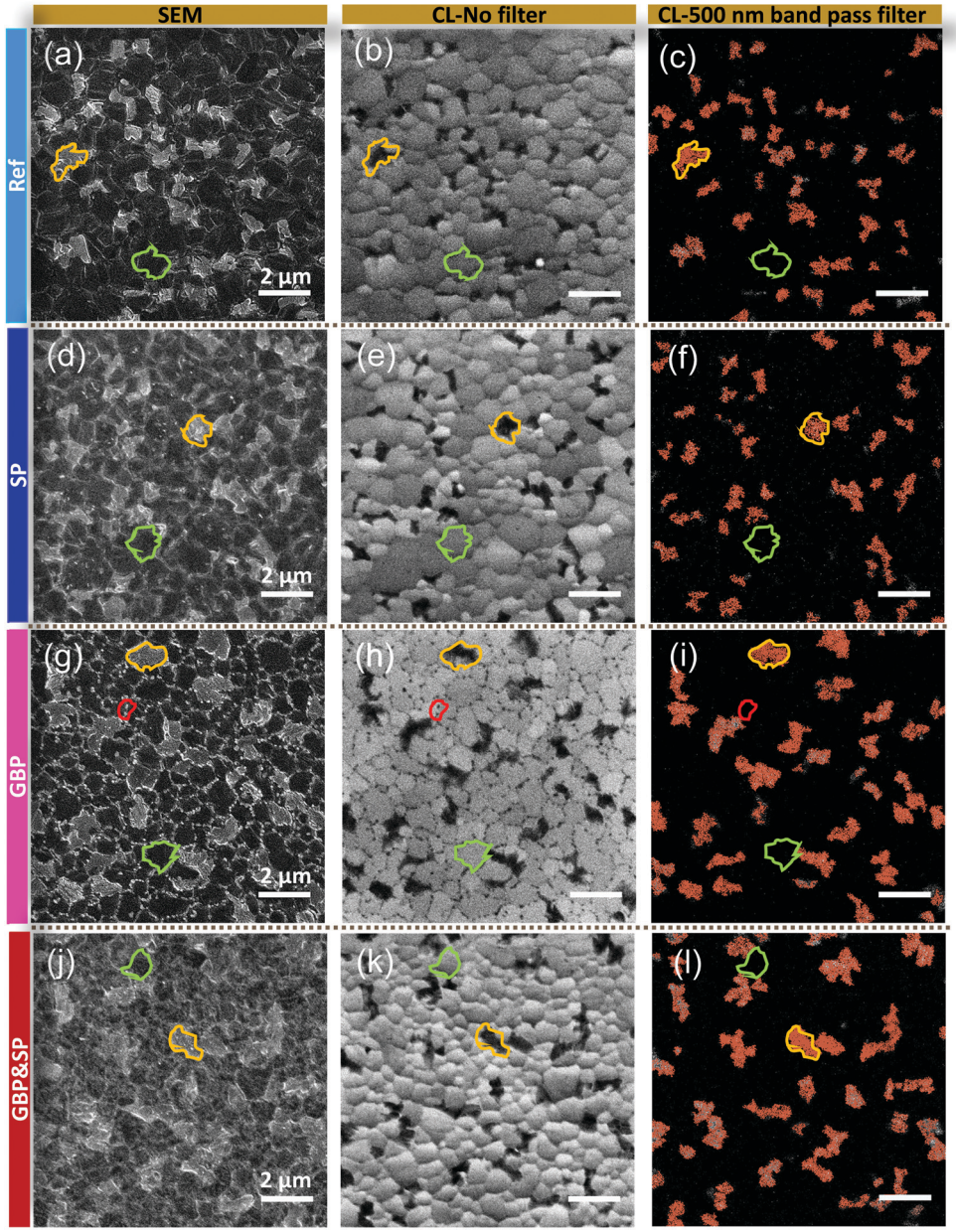

Fig. 4 Scanning electron microscopy (SEM) images, cathodoluminescence (CL) images recorded without any filter and CL images with bandpass (500 ± 40 nm) filter for perovskite absorbers prepared (a–c) without any modification (Ref), (d–f) with surface passivation (SP), (g–i) grain boundary passivation (GBP) and (j–l) grain boundary & surface passivation (GBP&SP), respectively. The green encircled grains represent the expected 3D perovskite phase with a bandgap of ~1.57 eV. The yellow encircled grains are attributed to PbI_2-rich crystallites. The small red encircled grains appear close to the grain boundaries for GBP films.

when we apply the 500 nm ± 40 nm bandpass filter, only the features related to PbI_2-rich grains can be observed, whereas no signal or feature correlated with the small bright grains is traceable (Fig. 4i). This indicates that these are not related to PbI_2 or $PbCl_2$. Finally, for GBP&SP film no small grains are visible in SEM anymore due to their dispersion after surface treatment (Fig. 4j) and thus can no longer be identified in the CL image either without or with the bandpass filter (Fig. 4k and l). Consistent with the PLQY and TRPL results, the GBP&SP film (Fig. 4k) exhibits the highest CL intensity at a wavelength of ~774 nm (Fig. S25, ESI†). This enhancement is attributed to the passivation of various recombination centres in the grain boundaries and/or at the surface of the perovskite layer.[126] Importantly, an additional CL peak at ~620 nm appears, which cannot be related to either the 3D perovskite phase or the PbI_2-rich phase. We find similar peaks in PL measurements of GBP&SP films as well as for SP films when using a higher PEACl concentration of 3 mg ml^{-1} (see Fig. S26, ESI†). We correlate this observation to the formation of a thin emissive 2D $(PEA)_2(Cs_yFA_{1-y})_{n-1}Pb_n(I_{1-x}Cl_x)_{3n+1}$ RP phase with $n = 2$ at the surface of the films, as will be discussed in the following.[75,127]

To analyse the crystal structure of our films, we perform X-ray diffraction (XRD) measurements (Fig. S27a, ESI†). All perovskite films exhibit the expected peaks at 14.2°, 20.1°, 24.6° and 28.4° from the (100), (110), (111) and (200) crystal planes of the 3D cubic α-$Cs_{0.18}FA_{0.82}PbI_3$ phase,[25,112,128] as well as a peak at ~12.9° related to PbI_2. The peak positions, intensities and FWHM of the XRD peaks are largely unchanged for SP films as observed in our previous work when using BABr for surface treatment.[59] For GBP films the intensity of the PbI_2 peak slightly increases (Fig. S27a, ESI†), in agreement with the larger number of PbI_2-rich crystallites observed in SEM and CL. Furthermore, the ratio of the (100) to (111) peak slightly decreases for GBP films as compared to Ref and SP films, implying a slightly less preferred (100) orientation of the perovskite grains (Fig. S27b, ESI†).[25,99] Similar to SP films, GBP&SP films exhibit a largely unchanged XRD spectrum as compared to GBP films. We do not observe a signal related to a 2D RP phase for the SP and GBP&SP films, which could be related to either the passivation layer being too thin to be detected by XRD, the presence of a heterogeneous distribution of $(PEA)_2(Cs_yFA_{1-y})_{n-1}Pb_n(I_{1-x}Cl_x)_{3n+1}$ phases with various n, or the presence of a non-crystalline PEA-based passivation layer.[14,59,68,69] Yet, upon further increasing the PEACl concentration to 4.5 mg ml^{-1} or 10 mg ml^{-1}, peaks at ~5.3°, 10.5°, 15.7°, 20.9°, 26.1° and 31.8° start to appear. These can be attributed to a pure 2D (n = 1) $(PEA)_2Pb(I_{1-x}Cl_x)_4$ RP phase with a superlattice spacing of ~1.7 nm that forms at the surface of the perovskite films (Fig. S28, ESI†).[77,129–132]

We perform XPS measurements of ITO/2PACz/perovskite stacks to get a better understanding of the elemental composition at the surface of our perovskite films and prove the presence of a PEACl-based passivation layer. For the Ref film, the XPS core-level spectra in Fig. 5a–c and Fig. S29a–c (ESI†) for the different elements in the 3D $Cs_{0.18}FA_{0.82}PbI_3$ absorber show the expected peaks with binding energies of ~138.7 eV (Pb $4f_{7/2}$), ~400.8 eV (N 1s), ~288.6 eV (C 1s from FA's N–C═N bonding), ~619.6 eV (I $3d_{5/2}$) and ~725.3 eV (Cs $3d_{5/2}$).[133] The additional C 1s peak at ~284.8 eV is attributed to adventitious carbon (sp^3 C–C bonding)

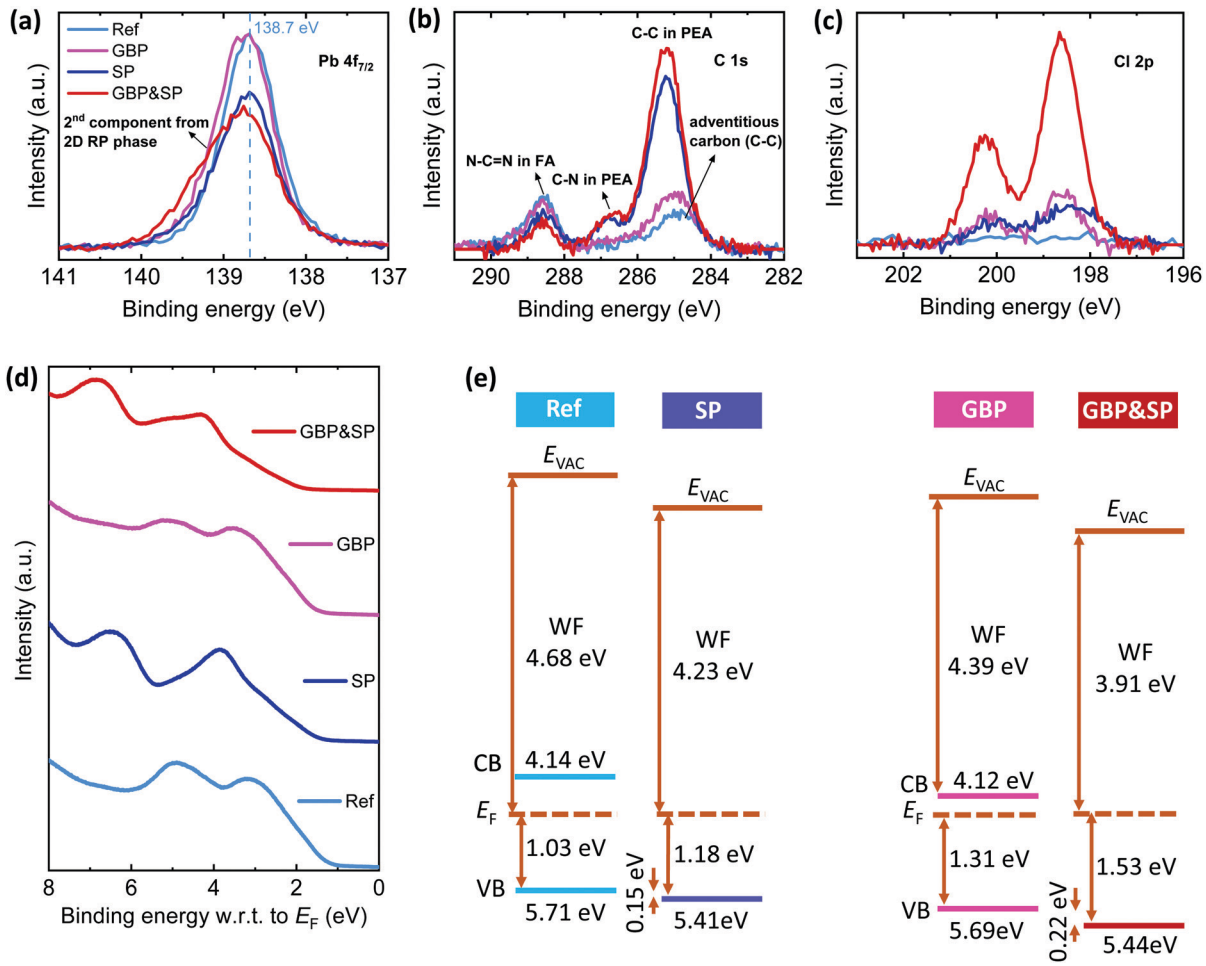

Fig. 5 X-ray photoelectron spectroscopy (XPS) spectra of (a) Pb $4f_{7/2}$, (b) C 1s and (c) Cl 2p core levels for perovskite films prepared on ITO/2PACz substrates without (Ref), with surface passivation (SP), grain boundary passivation (GBP), and grain boundary & surface passivation (GBP&SP) processes. (d) Proposed energy-level scheme based on ultraviolet photoelectron spectroscopy (UPS) measurements and (e) the respective spectra of the region close to the valence band onset. E_F is the Fermi level, E_{vac} is the vacuum level, and CB and VB show the conduction and valence band, respectively. The CB position of the 3D perovskite was calculated from the corresponding value of the optical gap.

at the film surface.[17,95] There is no signal related to a Cl 2p doublet at a binding energy of ~198.6 eV and ~200.2 eV despite using CsCl in the precursor solution which can be explained by the sublimation of FACl during the annealing process.[16,112,134] We note that we do not observe a peak related to metallic lead (Pb_0) at ~137 eV which emphasizes the high quality of our reference perovskite films.[19,20,74,87]

Upon PEACl:$PbCl_2$ incorporation and/or PEACl surface treatment (GBP, SP and GBP&SP films) there are three key observations as compared to the Ref film. Firstly, for BP films the Pb $4f_{7/2}$ core level slightly shifts toward higher binding energies and exhibits an increased FWHM, while for SP and GBP&SP films the signal intensity at ~138.7 eV decreases and the peak becomes broader and asymmetric toward the high-energy side. This asymmetry is stronger for GBP&SP films. Secondly, a Cl signal at ~198.6 eV (Cl $2p_{3/2}$) and ~200.2 eV (Cl $2p_{1/2}$) appears for all films, which is by far strongest for GBP&SP films. Thirdly, two new peaks at ~285.2 eV and 286.7 eV appear which are similar in intensity for SP and GBP&SP films and only very weak for GBP films. These peaks can be related to the C 1s emission from PEA (C–C and C–N bonds, respectively) with the expected stoichiometric ratio of 7 : 1.

Comparing SP and GBP&SP films using a higher PEACl concentration of 3 mg ml^{-1}, we find even more pronounced changes in the Pb 4f core levels (Fig. S30, ESI†). We stress that these are not accompanied by changes in the peak position or shape of the I $3d_{5/2}$, Cs $3d_{5/2}$ and C 1s core levels, which excludes the possibility of a shift due to electronic doping of the perovskite bulk.[87,95,135,136] We therefore relate the damping of the signal at ~138.7 eV for SP and GBP&SP, together with the appearance of a second Pb component at ~139.1 eV as well as a Cl 2p and PEA signal, to the formation of a thin PEACl-based passivation layer on the surface of the films that has a different chemical environment. The fact that for GBP the damping of the signal at ~138.7 eV is less pronounced and the peak becomes broader fits with our observation from SEM and CL that passivation happens mainly close to the grain boundary regions. To further test this interpretation, we show XPS measurements of SP and GBP&SP films with a much thicker passivation layer (10 mg ml^{-1}) in Fig. S31 (ESI†). A single Pb $4f_{7/2}$ peak at ~139.4 eV can be observed with no remaining signal at ~138.7 eV. In addition, no signals related to FA and Cs are observed anymore, which is an indication for the formation of a 2D RP phase with $n = 1$ and the composition $(PEA)_2Pb(I_{1-x}Cl_x)_4$, at the film surface that completely damps the Pb signal from the underlying 3D perovskite phase. This is in line with the appearance of the related XRD peaks discussed above. We note that the calculated atomic ratio of (I + Cl)/Pb is 4.71 (SP) and 5.14 (GBP&SP) and thus even larger than the expected 4, which could be related to excess PEAI or PEACl at the film surface possibly forming an amorphous phase as reported recently (see Table S4, ESI†).[14,68] Similar shifts of the Pb 4f binding energies have previously been observed when changing the halide, *i.e.* for $MAPbCl_3$ and $PbCl_2$ as compared to $MAPbI_3$ and PbI_2,[137,138] possibly due to the higher electronegativity of Cl as compared to I.

The formation of an $n = 1$ 2D RP phase has been proposed in several studies that employed PEAI or OAI for surface treatment.[14,61,65,67,70,77,79,80] However, for the thin passivation layer thicknesses studied in this work, the atomic ratio of Cs/Pb for SP and GBP&SP films first increases above the respective values for the Ref and GBP films (1.5 mg ml^{-1}), and only starts to slightly decrease for a higher PEACl concentration of 3 mg ml^{-1} (Table S4 and Fig. S32, ESI†). This indicates that Cs is taking part in the formation of the thin 2D RP passivation layer as otherwise the signal should be strictly decreasing because of the damping overlayer. This strict decrease in intensity with the formation of a 2D passivation layer can be seen for the atomic ratio of FA/Pb. This points towards a 2D RP $(PEA)_2(Cs_yFA_{1-y})_{n-1}Pb_n(I_{1-x}Cl_x)_{3n+1}$ phase with $y \rightarrow 1$ at the surface of our GBP, SP and GBP&SP films.[10,64,78,80,119,127,132] Another clear observation is that the intensity of the Cl 2p doublet is considerably higher for GBP&SP as compared to SP films (Fig. 5b), while the I $3d_{5/2}$ peak shows the reversed trend (Fig. S29c, ESI†). Accordingly, we note larger atomic ratios of Cl/Pb for GBP&SP *vs.* SP while the atomic ratio of I/Pb is smaller (Table S4 and Fig. S32, ESI†). This suggests that the 2D RP $(PEA)_2(Cs_yFA_{1-y})_{n-1}Pb_n(I_{1-x}Cl_x)_{3n+1}$ phase in case of GBP&SP films is more chloride-rich as compared to SP films ($x \rightarrow 1$). The hypothesis that an $n > 1$ 2D RP $(PEA)_2(Cs_yFA_{1-y})_{n-1}Pb_n(I_{1-x}Cl_x)_{3n+1}$ phase exist for all thin passivation layers is further corroborated by our observation of a CL and PL peak at ~620 nm for the SP (3 mg ml^{-1}) and GBP&SP films (see Fig. S25 and S26, ESI†) which points toward the existence of n of presumably 2.[75,127] To proof the existence of $n > 1$, we performed additional XRD measurements using a more sensitive setup. We specifically analyzed the low-angle region of the XRD spectrum ($2\theta < 12^\circ$) of GBP&SP films employing various concentrations of PEACL for surface treatment (3, 3.5, 4 and 4.5 mg ml^{-1}) and used the (100) peak of a GBP film as reference point. As shown in Fig. S33 (ESI†), for all GBP&SP films we observe a clear peak at ~5.1° and a corresponding one at ~10.2° that correlate to an $n = 1$ 2D RP phase, as well a small peak at ~3.8° that correlates to $n = 2$. Upon increasing the PEACL concentration, the intensity of the $n = 1$ peak monotonically increases, while that for $n = 2$ is comparable in intensity for the lower concentrations and only slightly in-creases for 4.5 mg ml^{-1}. Based on the XPS and XRD results together with the existence of a PL signal at ~620 nm as discussed above, we conclude that for thin passivation layers the surface consists of a mixture of $n = 1$ and $n = 2$ 2D RP phases, while for thicker passivation layers $n = 1$ becomes dominant toward the film surface. In order to give a rough estimate for the film thickness and n of the passivation layers, we take the Pb $4f_{7/2}$ peak which shows a clear indication for two phases and fit it with two components (see Fig. S34, ESI†): one for the 3D bulk phase (I) and one for the 2D RP surface phase (II). Here, for simplicity, we assume that the Pb $4f_{7/2}$ binding energy related to the 2D RP phase is situated at 139.1 eV. This allows to separate the relative contribution of the 2D (II) and 3D (I) material to the XPS signal and to evaluate the signal damping of the 3D bulk phase caused by the 2D RP overlayer. From here, we estimate a thickness of the 2D RP phase for a PEACl concentration of 1.5/3 mg ml^{-1} of ~0.7/2.4 nm for SP films and ~1.5/4.3 nm for

GBP&SP films (see Table S5 and further information in the XPS/UPS section in the ESI†). Finally, for simplicity assuming that the complete PEA signal measured in XPS is bound in a 2D RP phase, we can make a rough estimation of the respective n (averaged over the measured XPS spot) by analysing the atomic ratio of PEA to the 2D Pb (II) signal for 1.5/3 mg ml^{-1} PEACl (see Table S5, ESI†). We find that n for GBP&SP films ($\sim$2.6/2.3) is larger than for SP films ($\sim$1.2/1.7).

To assess the effect of the thin $(PEA)_2(Cs_yFA_{1-y})_{n-1}Pb_n(I_{1-x}Cl_x)_{3n+1}$ surface layer on the energetics of our films we perform UPS measurements. From the onsets of the secondary electron cut-off and valence band spectra (Fig. S35, ESI† and Fig. 5d) we derive the energy band diagrams shown in Fig. 5e. The Ref films exhibit a WF of 4.68 eV and an ionization potential (IP) of 5.71 eV which represents a slightly n-type perovskite film, in line with previous observations.[24,25,66,95,139] For GBP films, the WF considerably decreases to 4.39 eV while the IP stays roughly constant at 5.69 eV, implying that the perovskite becomes more n-type, which could be attributed to a reduced electron trap density, in line with our SCLC results, or a different surface termination.[24,25,66,106,140] The SP and GBP&SP films exhibit a further reduction in WF to 4.23 eV and 3.91 eV, respectively, together with a similar IP of 5.41 eV and 5.44 eV. These changes we attribute to the formation of the thin 2D RP phase with a larger bandgap and different chemical environments at the film surface as observed by CL and XPS. This is further supported by measurements of SP and GBP&SP films with a PEACl concentration of 3 mg ml^{-1}, for which the WF further decreases to 3.89 eV and 3.82 eV, while the IP exhibits similar values of 5.45 eV and 5.47 eV, which implies a valence band onset of 1.57 eV and 1.66 eV, respectively, the latter being larger than the 3D perovskite bandgap (Fig. S36, ESI†). We also note that the shape of the VB density of states clearly is affected by surface treatment (Fig. 5e), showing that the electronic properties of the 2D RP surface layer are different compared to the 3D bulk perovskite.[141] Therefore, in addition to the expected chemical passivation,[53] we speculate that the 2D RP phase at the film surface with an increased distance of the VB to the Fermi level results in hole blocking and thus a reduced probability for holes in the 3D perovskite absorber to recombine with electrons in the C_{60} layer.[25,53,72,86,142] In our case, electrons can effectively tunnel through the very thin ($\sim$0.7–1.5 nm) surface layer into C_{60},[25,38,142] resulting in still efficient charge extraction that allows very high FF for low PEACl concentrations of 1.5 mg ml^{-1}. For higher PEACl concentration of 3 mg ml^{-1} the passivation layers become too thick ($\sim$2.4–4.3 nm), making tunneling less likely which results in a decreased device performance due to a lower FF (Fig. S4, ESI†). Finally, we note that our results indicate band bending at the narrow 2D/3D interface as has recently been shown experimentally for the n–i–p architecture,[139,143] which also could contribute to the enhanced device performance.[10]

So far, our analyses clearly show that our dual passivation strategy effectively reduces non-radiative recombination mainly at the perovskite/C_{60} interface, but also the grain boundaries. Moreover, it is evident that a very thin 2D RP interlayer with a lower WF forms on the surface. The remaining questions are whether the PEACl:$PbCl_2$ additive passivates mainly defects in the grain interior and/or at the grain boundaries and how heterogeneous the surface passivation is for the different strategies. To shed light on this, we did frequency modulated Kelvin probe force microscopy (FM-KPFM) in the heterodyne KPFM implementation. KPFM measures the local contact potential difference (CPD) between a metallic tip and the sample surface and thus is directly related to the WF.[144,145] We used KPFM to map the effects of passivation on the CPD distribution of ITO/2PACz/perovskite/C_{60} layer stacks, especially looking at grain boundaries, PbI_2-rich grains and extent of heterogeneity (see Fig. 6). We want to stress that KPFM is prone to crosstalk from topography, often leading to KPFM contrast in strongly curved surface regions, such as grain boundaries. To minimize crosstalk artefacts, we use FM-KPFM[146] and carefully analysed the images, comparing the KPFM signal with the topography at the grain boundaries.

The map for the Ref sample (Fig. 6a) shows perovskite grains with a rather uniform CPD of (-430 ± 40) mV interrupted by grains with a less uniform and $\sim$110–230 mV lower CPD. The size and the surface distribution of the darker regions correspond to the PbI_2-rich grains as observed in SEM and CL (Fig. 4 and Fig. S19, ESI†). Here, the negative CPD contrast could be explained by a higher WF in PbI_2 as compared to the 3D perovskite due to its larger bandgap and p-type characteristics,[137,147–149] in line with previous observations.[150,151] The map of the GBP sample (Fig. 6b) shows a similar trend in CPD contrast between more homogeneous perovskite grains with a CPD of (-700 ± 120) mV and less uniform spots with a CPD of (-1300 ± 280) mV. We note that the absolute value of the CPD depends on the tip's WF, which is sensitive to tip wear and contamination during the scanning. This could explain the overall lower absolute CPD in the GBP films. Assuming that the PbI_2 covered regions for the Ref and GBP sample have a comparable WF, we can use these ''dark'' regions as internal reference surface. Therefore, we first compare the relative change of the CPD value at the 3D perovskite grains with that at the dark PbI_2-rich grains for the Ref as compared to the GBP samples, *i.e.* $\Delta CPD_{3D\text{-}PbI2}$ ($CPD_{3D\text{-}grains}$–$CPD_{PbI2\text{-}grains}$). For the Ref sample $\Delta CPD_{3D\text{-}PbI2}$ is $\sim$170 mV, while it is $\sim$600 mV for the GBP sample (note the different scales in Fig. 6a and b). This relative difference of $\Delta CPD_{3D\text{-}PbI2}$ of $\sim$430 mV is comparable with the reduction in WF of $\sim$290 mV for GBP films as determined by UPS. Therefore, we attribute this observation to the fact that the PEACl:$PbCl_2$ additive mainly lowers the WF of the 3D perovskite grains, while the PbI_2-rich grains are not modified by this strategy.

To analyse if the CPD at the grain boundaries with respect to the grain interior is modified for the GBP sample as compared to the Ref sample, *i.e.*, ΔCPD_{GB} ($CPD_{grain\ boundary}$–CPD_{grain}), we show line profiles across representative grain boundaries in Fig. S37a and b (ESI†). To allow for a direct comparison, we shifted the CPD values of the grain interior at different positions to zero. For the Ref sample, many of the grain boundaries show a $\sim$50–100 mV lower CPD compared to the grains, similarly as

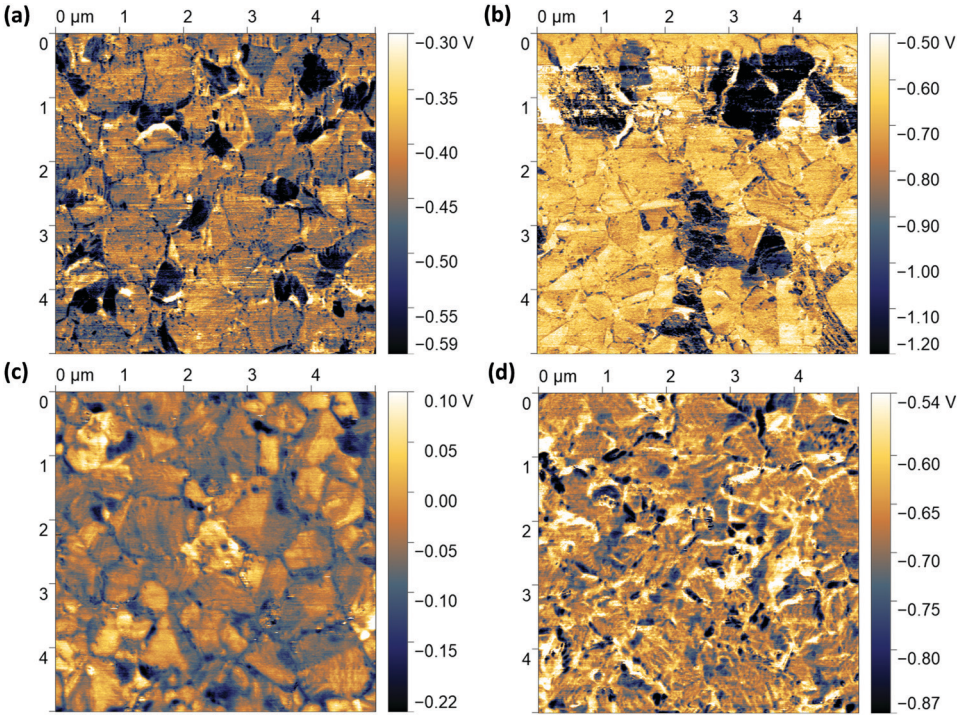

Fig. 6 Kelvin pobe force microscopy (KPFM) images for perovskite films with the structure ITO/2PACz/perovskite/C_{60} prepared (a) without any modification (Ref), (b) with grain boundary passivation (GBP), (c) surface passivation (SP), and (d) grain boundary & surface passivation (GBP&SP) processes.

previously reported.[152–155] Such observations have been generally attributed to an enhanced ion and/or defect density, possibly due to a lower energy for defect formation at grain boundary regions.[42,46,154] In contrast, for the GBP sample we observed on average less contrast between grain boundaries and grain interior such that some of them cannot be clearly distinguished in the CPD map and line profiles anymore. We analysed in total a larger number of grain boundaries (~60) (Fig. S38a and b, ESI†) for better statistics and found an average reduction from ~93 mV to ~74 mV for the GBP as compared to the Ref sample together with a large number of grain boundaries not showing any CPD contrast (see histogram in Fig. S38c, ESI†). A reduction in ΔCPD_{GB} for the GBP as compared to the Ref sample indicates that the PEACl:$PbCl_2$ additive could specifically passivate the grain boundaries, resulting in a slightly more pronounced reduction of the WF with respect to the PbI_2-rich grains as compared to the grain interior. We hypothesize that this is due to the formation of a PEACl-based 2D RP $(PEA)_2(Cs_yFA_{1-y})_{n-1}Pb_n(I_{1-x}Cl_x)_{3n+1}$ phase specifically close to the grain boundaries, in line with the observations from CL and XPS.

We further analyse the effects of PEACl surface treatment on the CPD (Fig. 6c and d). The SP Sample shows a heterogeneous CPD of (−52 ± 50) mV with no clear distinction between high- and low-CPD grains anymore; however, we still observe a slight grain boundary contrast. We attribute this to the very thin 2D RP phase on top of the perovskite film – as identified by XPS – that changes the electrical properties of the film surface, including the regions of the PbI_2-rich grains. We speculate that PEACl cannot completely penetrate and thus passivate the grain boundary regions, explaining why we still observe a CPD contrast. The enhanced heterogeneity of the CPD over different grains as compared to the Ref sample could be explained by the fact that the 2D RP $(PEA)_2(Cs_yFA_{1-y})_{n-1}Pb_n(I_{1-x}Cl_x)_{3n+1}$ phase exhibits various n, *i.e.* a mixture of $n = 1$ and $n = 2$ phases with slightly different WF at different regions of the films. For the GBP&SP samples, we observe an even more heterogeneous CPD of (−670 ± 70) mV compared to all other samples (Fig. 6d and Fig. S39, ESI†). Critically, no grain boundaries and PbI_2-rich grains can be identified in the CPD map anymore. Taking the CL, XPS and KPFM results together, this indicates that employing both PEACl:$PbCl_2$ as additive and PEACl for surface treatment leads to a thin heterogeneous 2D RP $(PEA)_2(Cs_yFA_{1-y})_{n-1}Pb_n(I_{1-x}Cl_x)_{3n+1}$ phase at the grain boundaries and surface of the perovskite film with n of ~1–2. Finally, we note that the CPD value can be affected both by the facet orientation as well as the existence of RP phases with various n, which makes it difficult to disentangle these effects in detail.[146,153,156–158]

Stability of passivated PSCs

Defect sites at grain boundaries and surfaces accelerate the degradation of perovskite thin films, since defects facilitate the migration of charged defects and mobile ions.[25,73,159,160] Having demonstrated that our dual passivation strategy reduces defects at the grain boundaries and the surface of the perovskite film, the question arises whether the concept also serves to increase the stability, *i.e.* slows down the degradation of the perovskite films. For this purpose, we compare the activation energy for ion

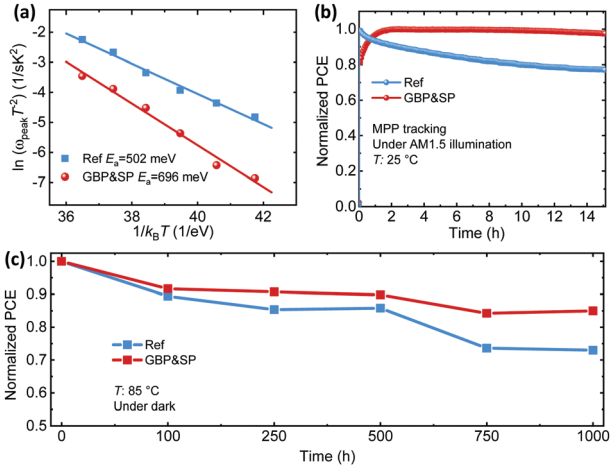

Fig. 7 (a) Arrhenius plots determined from the derivative of admittance spectra to determine the activation energy (E_a) for reference (Ref) and grain boundary & surface passivation (GBP&SP) perovskite solar cells. (b) Maximum power point (MPP) tracking of the Ref and GBP&SP perovskite solar cells under continuous solar illumination (100 mW cm^{-2}) in a nitrogen atmosphere. (c) Thermal stability of devices heated at temperature of 85 °C in dark condition inside of a glovebox. Data points were extracted from *J*–*V* curves at various time intervals.

migration for Ref, SP, GBP and GBP&SP PSCs by thermal admittance spectroscopy (TAS). Fig. S40a–d (ESI†) depicts the TAS spectra of the lateral devices measured from 278 to 318 K in the dark. The activation energy (E_a) is obtained from the Arrhenius plot using the equation $\omega_{peak} = \beta T^2 \exp(-E_a/k_B T)$, where β is temperature independent prefactor, T is the absolute temperature, k_B is the Boltzmann constant, and ω_{peak} is the angular frequency obtained by the maxima of the capacitance logarithmic derivative (Fig. S40e–h, ESI†). In line with the previously discussed trends, the GBP&SP PSCs exhibit by far the highest E_a of 696 meV, surpassing the activation energy for either single passivation strategy (GBP: 580 meV, SP: 551 meV) as well as the Ref PSC (502 meV) (Fig. 7a and Fig. S41, ESI†). The trend in E_a indicates that the simultaneous passivation of grain boundaries and the surface of the perovskite film yields by far the highest energy barrier for ion migration. As a consequence, the accumulation of ionic defects is most effectively suppressed for GBP&SP PSCs. To verify that the reduced ion migration also implies enhanced device stability under illumination,[90,100] the operational stability of GBP&SP and Ref PSCs is examined under constant illumination (100 mW cm^{-2}, AM1.5G, 14 h, room temperature) and MPP tracking conditions. The PCE of the Ref PSC decreases to around 80% of the initial value after only 8 h, whereas the GBP&SP PSC retained almost 98% of the initial PCE after 14 h (Fig. 7b). Furthermore, we investigate the operational stability of PSCs for which the perovskite/ETL interface is passivated using a thin evaporated LiF layer, which is often employed in high-efficiency p–i–n PSCs.[31,35,38,88,89,93] In comparison with our GBP&SP PSCs (Fig. S42, ESI†) the p–i–n PSC with LiF passivation layer degrades much faster, reaching 80% of the initial PCE already after 7 h of constant illumination. Similar reports on the fast degradation of LiF containing p–i–n PSC can be found in literature.[31,93] Next to improved operational stability under constant AM1.5G illumination, the GBP&SP PSCs demonstrate improved thermal stability as compared to Ref PSCs by tracking the photovoltaic performance of the devices after aging under 85 °C heating in the dark over 1000 h (see Fig. 7c). To further evaluate the stability with regard to moisture, we exposed unencapsulated Ref PSCs and GBP&SP PSCs to a relative humidity of ~50% in ambient atmosphere and at room temperature for 1 day. The photographs and absorption data exhibit no changes for the GBP&SP film, while the Ref film is entirely decomposed to PbI_2 (Fig. S43a, ESI†). The increased contact angle of water droplets from 55.9° for the Ref film to 78° for the GBP&SP film (Fig. S43b, ESI†) confirms the better moisture resistance capability in the case of GBP&SP, which is attributed to the presence of hydrophobic PEA+ cations at the surface and grain boundaries of the perovskite films that acts as a hydrophobic barrier.[25,71,76] We note that the formation of shallow iodine interstitials upon passivation with iodide-based passivation molecules has recently been proposed to cause accelerated degradation of $FAPbI_3$ perovskites.[71] Our chloride-based dual passivation approach might potentially mitigate this issue. In summary, the presented fundamental assessment of stability for PSCs employing our dual passivation strategy highlights the importance of passivating defects at both the surface and the grain boundaries of perovskite films for achieving PCSs exhibiting both high efficiency and stability.

Conclusion

In summary, we demonstrate a dual passivation strategy for p–i–n PSCs that simultaneously passivates defects at the perovskite/C_{60} interface as well as in the grain boundaries using the long chain alkylammonium salt phenethylammonium chloride. We achieve a substantial enhancement in charge carrier lifetime and quasi-Fermi level splitting compared to reference films as well as to films with either individual grain boundary or surface passivation. The best PSC with dual passivation achieves a significant absolute enhancement in both V_{OC} (76 mV) and FF (4.6%) compared to the best reference device. As a result, a remarkable stabilized PCE of 22.3% is demonstrated, one of the highest reported for p–i–n PSCs. We attribute this improvement in performance to the formation of a heterogeneous 2D RP $(PEA)_2(Cs_yFA_{1-y})_{n-1}Pb_n(I_{1-x}Cl_x)_{3n+1}$ phase with $n \sim 1$–2 at the surface and grain boundaries of the films, which leads to (1) efficient chemical passivation of grain boundary and surface/interface defects and (2) additional hole blocking at the perovskite/C_{60} interface. Finally, we demonstrate that the activation energy for ion migration is strongly increased upon dual passivation, which is reflected by an enhanced device stability under maximum power point (MPP) tracking and prolonged heat treatment. This work highlights the importance of defect management by employing a proper material both for grain boundary as well as surface passivation for achieving high-efficiency and stable inverted p–i–n PSCs. Thereby this work makes a relevant contribution to the advance of perovskite-based flexible and tandem photovoltaics.

Author contributions

S. G. conceived the initial idea for this study and developed it further with support of P. F., I. M. H. and U. W. P. Furthermore, S. G. designed the experiments, fabricated the perovskite films and performed the *J–V*, EQE and long-term stability measurements. P. F. performed the absolute and intensity-dependent PLQY measurements and data analysis. I. M. H. performed the transient photoluminescence measurements and data analysis. S. G. performed the XRD measurements. M. F. performed the XPS/UPS measurements and data analysis and P. F. and J. P. H. supported in data interpretation. M. S. helped for device fabrication. P. R. performed the KPFM measurements, supervised by S. A. L. W., and the data was analysed by P. R., S. G., P. F. and S. A. L. W. The CL measurements were performed by T. D. The TAS measurements were performed by S. G. and M. R. K., and O. A. and M. R. K. analysed the data. T. A. and B. A. N. performed the SEM measurements. F. S. performed the contact angle measurement. T. F. applied and optimized the antireflection coating. R. S. helped for long-term stability measurement. B. A. N. helped with designing the schematics. D. F. performed additional high-resolution XRD measurements. U. L. and U. W. P. supervised the whole project. S. G., P. F. and U. W. P. drafted the manuscript. All authors reviewed and commented on the paper.

Conflicts of interest

There are no conflicts to declare.

Acknowledgements

B. A. N. acknowledges the financial support from the European Union's Horizon 2020 research and innovation program under the Marie Skłodowska-Curie grant agreement No [840937]. T. D. acknowledges the financial support from Australian Centre for Advanced Photovoltaics (ACAP). O. A. acknowledges the funding from the European Union's Horizon 2020 research and innovation program under the Photonics Public Private Partnership (www.photonics21.org) with the project PEROXIS (grant no. 871336). M. S. acknowledges funding from the European Research Council (ERC) under the European Union's Horizon 2020 research and innovation program (Grant agreement No. 947221). Financial support by the Initiating and Networking funding of the Helmholtz Association (HYIG of U. W. P. (VHNG-1148)), the Helmholtz Energy Materials Foundry (HEMF), PEROSEED (ZT0024), the German Federal Ministry for Economic Affairs (BMWi) through the project 27Plus6 (03EE1056B) as well as the project CAPITANO (03EE1038B), and the Karlsruhe School of Optics & Photonics (KSOP) is gratefully acknowledged. Furthermore, this project has received funding from the European Union's Horizon 2020 research and innovation program under grant agreement No 850937 (PERCISTAND). The financial support of this research through the Baden-Württemberg Foundation is acknowledged (project acronym: ANU-KIT-PV).

References

1 NREL Best Research-Cell Efficiency Chart, https://www.nrel.gov/pv/cell-efficiency.html, accessed: March 2021.
2 O. Almora, D. Baran, G. C. Bazan, C. Berger, C. I. Cabrera, K. R. Catchpole, S. Erten-Ela, F. Guo, J. Hauch, A. W. Y. Ho-Baillie, T. J. Jacobsson, R. A. J. Janssen, T. Kirchartz, N. Kopidakis, Y. Li, M. A. Loi, R. R. Lunt, X. Mathew, M. D. McGehee, J. Min, D. B. Mitzi, M. K. Nazeeruddin, J. Nelson, A. F. Nogueira, U. W. Paetzold, N. Park, B. P. Rand, U. Rau, H. J. Snaith, E. Unger, L. Vaillant-Roca, H. Yip and C. J. Brabec, *Adv. Energy Mater.*, 2021, **11**, 2002774.
3 G. Kim, H. Min, K. S. Lee, D. Y. Lee, S. M. Yoon and S. Il Seok, *Science*, 2020, **370**, 108–112.
4 M. Jeong, I. W. Choi, E. M. Go, Y. Cho, M. Kim, B. Lee, S. Jeong, Y. Jo, H. W. Choi, J. Lee, J. Bae, S. K. Kwak, D. S. Kim and C. Yang, *Science*, 2020, **1620**, 1615–1620.
5 M. Kim, G. Kim, T. K. Lee, I. W. Choi, H. W. Choi, Y. Jo, Y. J. Yoon, J. W. Kim, J. Lee, D. Huh, H. Lee, S. K. Kwak, J. Y. Kim and D. S. Kim, *Joule*, 2019, **3**, 2179–2192.
6 E. H. Jung, N. J. Jeon, E. Y. Park, C. S. Moon, T. J. Shin, T. Y. Yang, J. H. Noh and J. Seo, *Nature*, 2019, **567**, 511–515.
7 H. Zhu, Y. Ren, L. Pan, O. Ouellette, F. T. Eickemeyer, Y. Wu, X. Li, S. Wang, H. Liu, X. Dong, S. M. Zakeeruddin, Y. Liu, A. Hagfeldt and M. Grätzel, *J. Am. Chem. Soc.*, 2021, **143**, 3231–3237.
8 M. A. Mahmud, T. Duong, Y. Yin, J. Peng, Y. Wu, T. Lu, H. T. Pham, H. Shen, D. Walter, H. T. Nguyen, N. Mozaffari, G. D. Tabi, Y. Liu, G. Andersson, K. R. Catchpole, K. J. Weber and T. P. White, *Small*, 2020, **16**, 2005022.
9 T.-S. Su, F. T. Eickemeyer, M. A. Hope, F. Jahanbakhshi, M. Mladenović, J. Li, Z. Zhou, A. Mishra, J.-H. Yum, D. Ren, A. Krishna, O. Ouellette, T.-C. Wei, H. Zhou, H.-H. Huang, M. D. Mensi, K. Sivula, S. M. Zakeeruddin, J. V. Milić, A. Hagfeldt, U. Rothlisberger, L. Emsley, H. Zhang and M. Grätzel, *J. Am. Chem. Soc.*, 2020, **142**, 19980–19991.
10 J. J. Yoo, S. Wieghold, M. C. Sponseller, M. R. Chua, S. N. Bertram, N. T. P. Hartono, J. S. Tresback, E. C. Hansen, J.-P. Correa-Baena, V. Bulović, T. Buonassisi, S. S. Shin and M. G. Bawendi, *Energy Environ. Sci.*, 2019, **12**, 2192–2199.
11 B. Yang, J. Suo, E. Mosconi, D. Ricciarelli, W. Tress, F. De Angelis, H. Kim and A. Hagfeldt, *ACS Energy Lett.*, 2020, **5**, 3159–3167.
12 J. Jeong, M. Kim, J. Seo, H. Lu, P. Ahlawat, A. Mishra, Y. Yang, M. A. Hope, F. T. Eickemeyer, M. Kim, Y. J. Yoon, I. W. Choi, B. P. Darwich, S. J. Choi, Y. Jo, J. H. Lee, B. Walker, S. M. Zakeeruddin, L. Emsley, U. Rothlisberger, A. Hagfeldt, D. S. Kim, M. Grätzel and J. Y. Kim, *Nature*, 2021, **592**, 381–385.
13 J. J. Yoo, G. Seo, M. R. Chua, T. G. Park, Y. Lu, F. Rotermund, Y. Kim, C. S. Moon, N. J. Jeon, J.-P. Correa-Baena, V. Bulović, S. S. Shin, M. G. Bawendi and J. Seo, *Nature*, 2021, **590**, 587–593.

14 Q. Jiang, Y. Zhao, X. Zhang, X. Yang, Y. Chen, Z. Chu, Q. Ye, X. Li, Z. Yin and J. You, *Nat. Photonics*, 2019, **13**, 460–466.
15 P. Wang, R. Li, B. Chen, F. Hou, J. Zhang, Y. Zhao and X. Zhang, *Adv. Mater.*, 2020, **32**, 1905766.
16 C. Ma and N.-G. Park, *ACS Energy Lett.*, 2020, **5**, 3268–3275.
17 X. Yang, Y. Fu, R. Su, Y. Zheng, Y. Zhang, W. Yang, M. Yu, P. Chen, Y. Wang, J. Wu, D. Luo, Y. Tu, L. Zhao, Q. Gong and R. Zhu, *Adv. Mater.*, 2020, **32**, 2002585.
18 E. H. Jung, B. Chen, K. Bertens, M. Vafaie, S. Teale, A. Proppe, Y. Hou, T. Zhu, C. Zheng and E. H. Sargent, *ACS Energy Lett.*, 2020, **5**, 2796–2801.
19 Q. Jiang, Z. Ni, G. Xu, Y. Lin, P. N. Rudd, R. Xue, Y. Y. Li, Y. Y. Li, Y. Gao and J. Huang, *Adv. Mater.*, 2020, **32**, 2001581.
20 X. Yang, D. Luo, Y. Xiang, L. Zhao, M. Anaya, Y. Shen, J. Wu, W. Yang, Y. H. Chiang, Y. Tu, R. Su, Q. Hu, H. Yu, G. Shao, W. Huang, T. P. Russell, Q. Gong, S. D. Stranks, W. Zhang and R. Zhu, *Adv. Mater.*, 2021, **33**, 2006435.
21 J. Zhuang, P. Mao, Y. Luan, N. Chen, X. Cao, G. Niu, F. Jia, F. Wang, S. Cao and J. Wang, *Adv. Funct. Mater.*, 2021, **31**, 2010385.
22 H. Lu, Y. Liu, P. Ahlawat, A. Mishra, W. R. Tress, F. T. Eickemeyer, Y. Yang, F. Fu, Z. Wang, C. E. Avalos, B. I. Carlsen, A. Agarwalla, X. Zhang, X. Li, Y. Zhan, S. M. Zakeeruddin, L. Emsley, U. Rothlisberger, L. Zheng, A. Hagfeldt and M. Grätzel, *Science*, 2020, **370**, eabb8985.
23 M. Green, E. Dunlop, J. Hohl-Ebinger, M. Yoshita, N. Kopidakis and X. Hao, *Prog. Photovoltaics*, 2021, **29**, 3–15.
24 F. Li, X. Deng, F. Qi, Z. Li, D. Liu, D. Shen, M. Qin, S. Wu, F. Lin, S. Jang, J. Zhang, X. Lu, D. Lei, C. Lee, Z. Zhu and A. K.-Y. Jen, *J. Am. Chem. Soc.*, 2020, **142**, 20134–20142.
25 X. Zheng, Y. Hou, C. Bao, J. Yin, F. Yuan, Z. Huang, K. Song, J. Liu, J. Troughton, N. Gasparini, C. Zhou, Y. Lin, D.-J. Xue, B. Chen, A. K. Johnston, N. Wei, M. N. Hedhili, M. Wei, A. Y. Alsalloum, P. Maity, B. Turedi, C. Yang, D. Baran, T. D. Anthopoulos, Y. Han, Z.-H. Lu, O. F. Mohammed, F. Gao, E. H. Sargent and O. M. Bakr, *Nat. Energy*, 2020, **5**, 131–140.
26 W. Wu, P. N. Rudd, Q. Wang, Z. Yang and J. Huang, *Adv. Mater.*, 2020, **32**, 2000995.
27 S. Wu, J. Zhang, Z. Li, D. Liu, M. Qin, S. H. Cheung, X. Lu, D. Lei, S. K. So, Z. Zhu and A. K.-Y. Jen, *Joule*, 2020, **4**, 1248–1262.
28 X. Sun, Z. Li, X. Yu, X. Wu, C. Zhong, D. Liu, D. Lei, A. K.-Y. Jen, Z. Li and Z. Zhu, *Angew. Chem., Int. Ed.*, 2021, **60**, 7227–7233.
29 X. Hu, C. Liu, Z. Zhang, X. Jiang, J. Garcia, C. Sheehan, L. Shui, S. Priya, G. Zhou, S. Zhang and K. Wang, *Adv. Sci.*, 2020, **7**, 2001285.
30 A. Y. Alsalloum, B. Turedi, K. Almasabi, X. Zheng, R. Naphade, S. D. Stranks, O. F. Mohammed and O. M. Bakr, *Energy Environ. Sci.*, 2021, **14**, 2263–2268.
31 A. Al-Ashouri, E. Köhnen, B. Li, A. Magomedov, H. Hempel, P. Caprioglio, J. A. Márquez, A. B. Morales Vilches, E. Kasparavicius, J. A. Smith, N. Phung, D. Menzel, M. Grischek, L. Kegelmann, D. Skroblin, C. Gollwitzer, T. Malinauskas, M. Jošt, G. Matič, B. Rech, R. Schlatmann, M. Topič, L. Korte, A. Abate, B. Stannowski, D. Neher, M. Stolterfoht, T. Unold, V. Getautis and S. Albrecht, *Science*, 2020, **370**, 1300–1309.
32 A. Al-Ashouri, A. Magomedov, M. Roß, M. Jošt, M. Talaikis, G. Chistiakova, T. Bertram, J. A. Márquez, E. Köhnen, E. Kasparavičius, S. Levcenco, L. Gil-Escrig, C. J. Hages, R. Schlatmann, B. Rech, T. Malinauskas, T. Unold, C. A. Kaufmann, L. Korte, G. Niaura, V. Getautis and S. Albrecht, *Energy Environ. Sci.*, 2019, **12**, 3356–3369.
33 X. Lin, D. Cui, X. Luo, C. Zhang, Q. Han, Y. Wang and L. Han, *Energy Environ. Sci.*, 2020, **13**, 3823–3847.
34 M. Stolterfoht, M. Grischek, P. Caprioglio, C. M. Wolff, E. Gutierrez-Partida, F. Peña-Camargo, D. Rothhardt, S. Zhang, M. Raoufi, J. Wolansky, M. Abdi-Jalebi, S. D. Stranks, S. Albrecht, T. Kirchartz and D. Neher, *Adv. Mater.*, 2020, **32**, 2000080.
35 M. Stolterfoht, P. Caprioglio, C. M. Wolff, J. A. Márquez, J. Nordmann, S. Zhang, D. Rothhardt, U. Hörmann, Y. Amir, A. Redinger, L. Kegelmann, F. Zu, S. Albrecht, N. Koch, T. Kirchartz, M. Saliba, T. Unold and D. Neher, *Energy Environ. Sci.*, 2019, **12**, 2778–2788.
36 D. Luo, R. Su, W. Zhang, Q. Gong and R. Zhu, *Nat. Rev. Mater.*, 2020, **5**, 44–60.
37 C. M. Wolff, P. Caprioglio, M. Stolterfoht and D. Neher, *Adv. Mater.*, 2019, **31**, 1902762.
38 M. Stolterfoht, C. M. Wolff, J. A. Márquez, S. Zhang, C. J. Hages, D. Rothhardt, S. Albrecht, P. L. Burn, P. Meredith, T. Unold and D. Neher, *Nat. Energy*, 2018, **3**, 847–854.
39 S. Zhang, P. E. Shaw, G. Zhang, H. Jin, M. Tai, H. Lin, P. Meredith, P. L. Burn, D. Neher and M. Stolterfoht, *ACS Appl. Mater. Interfaces*, 2020, **12**, 37647–37656.
40 J.-W. Lee, S.-H. Bae, N. De Marco, Y.-T. Hsieh, Z. Dai and Y. Yang, *Mater. Today Energy*, 2018, **7**, 149–160.
41 A. Castro-Méndez, J. Hidalgo and J. Correa-Baena, *Adv. Energy Mater.*, 2019, **9**, 1901489.
42 J.-S. Park and A. Walsh, *Annu. Rev. Condens. Matter Phys.*, 2021, **12**, 042020annurev-conmatphys-.
43 Y. Shao, Y. Fang, T. Li, Q. Wang, Q. Dong, Y. Deng, Y. Yuan, H. Wei, M. Wang, A. Gruverman, J. Shield and J. Huang, *Energy Environ. Sci.*, 2016, **9**, 1752–1759.
44 J. S. Yun, J. Seidel, J. Kim, A. M. Soufiani, S. Huang, J. Lau, N. J. Jeon, S. Il Seok, M. A. Green and A. Ho-Baillie, *Adv. Energy Mater.*, 2016, **6**, 1600330.
45 L. Liu, S. Huang, Y. Lu, P. Liu, Y. Zhao, C. Shi, S. Zhang, J. Wu, H. Zhong, M. Sui, H. Zhou, H. Jin, Y. Li and Q. Chen, *Adv. Mater.*, 2018, **30**, 1800544.
46 N. Phung, A. Al-Ashouri, S. Meloni, A. Mattoni, S. Albrecht, E. L. Unger, A. Merdasa and A. Abate, *Adv. Energy Mater.*, 2020, **10**, 1903735.
47 L. McGovern, I. Koschany, G. Grimaldi, L. A. Muscarella and B. Ehrler, *J. Phys. Chem. Lett.*, 2021, 2423–2428.
48 S. P. Dunfield, L. Bliss, F. Zhang, J. M. Luther, K. Zhu, M. F. A. M. Hest, M. O. Reese and J. J. Berry, *Adv. Energy Mater.*, 2020, **10**, 1904054.

49 L. Fu, H. Li, L. Wang, R. Yin, B. Li and L.-W. Yin, *Energy Environ. Sci.*, 2020, **13**, 4017–4056.
50 Q. Sun, P. Fassl, D. Becker-Koch, A. Bausch, B. Rivkin, S. Bai, P. E. Hopkinson, H. J. Snaith and Y. Vaynzof, *Adv. Energy Mater.*, 2017, **7**, 1700977.
51 J. P. Bastos, G. Uytterhoeven, W. Qiu, U. W. Paetzold, D. Cheyns, S. Surana, J. Rivas, M. Jaysankar, W. Song, T. Aernouts, J. Poortmans and R. Gehlhaar, *ACS Appl. Mater. Interfaces*, 2019, **11**, 16517–16526.
52 S. Akin, N. Arora, S. M. Zakeeruddin, M. Grätzel, R. H. Friend and M. I. Dar, *Adv. Energy Mater.*, 2020, **10**, 1903090.
53 E. Aydin, M. Bastiani and S. Wolf, *Adv. Mater.*, 2019, **31**, 1900428.
54 F. Gao, Y. Zhao, X. Zhang and J. You, *Adv. Energy Mater.*, 2020, **10**, 1902650.
55 H. Zhang, M. K. Nazeeruddin and W. C. H. Choy, *Adv. Mater.*, 2019, **31**, 1805702.
56 W. Qi, X. Zhou, J. Li, J. Cheng, Y. Li, M. J. Ko, Y. Zhao and X. Zhang, *Sci. Bull.*, 2020, **65**, 2022–2032.
57 Y. Li, H. Wu, W. Qi, X. Zhou, J. Li, J. Cheng, Y. Zhao, Y. Li and X. Zhang, *Nano Energy*, 2020, **77**, 105237.
58 S. Akin, B. Dong, L. Pfeifer, Y. Liu, M. Graetzel and A. Hagfeldt, *Adv. Sci.*, 2021, **8**, 2004593.
59 S. Gharibzadeh, B. Abdollahi Nejand, M. Jakoby, T. Abzieher, D. Hauschild, S. Moghadamzadeh, J. A. Schwenzer, P. Brenner, R. Schmager, A. A. Haghighirad, L. Weinhardt, U. Lemmer, B. S. Richards, I. A. Howard and U. W. Paetzold, *Adv. Energy Mater.*, 2019, **9**, 1803699.
60 S. Gharibzadeh, I. M. Hossain, P. Fassl, B. A. Nejand, T. Abzieher, M. Schultes, E. Ahlswede, P. Jackson, M. Powalla, S. Schäfer, M. Rienäcker, T. Wietler, R. Peibst, U. Lemmer, B. S. Richards and U. W. Paetzold, *Adv. Funct. Mater.*, 2020, **30**, 1909919.
61 Y. Liu, S. Akin, L. Pan, R. Uchida, N. Arora, J. V. Milić, A. Hinderhofer, F. Schreiber, A. R. Uhl, S. M. Zakeeruddin, A. Hagfeldt, M. I. Dar and M. Grätzel, *Sci. Adv.*, 2019, **5**, eaaw2543.
62 Z. Li, J. Zhang, S. Wu, X. Deng, F. Li, D. Liu, C. Lee, F. Lin, D. Lei, C.-C. Chueh, Z. Zhu and A. K. Y. Jen, *Nano Energy*, 2020, **78**, 105377.
63 M. A. Mahmud, T. Duong, Y. Yin, H. T. Pham, D. Walter, J. Peng, Y. Wu, L. Li, H. Shen, N. Wu, N. Mozaffari, G. Andersson, K. R. Catchpole, K. J. Weber and T. P. White, *Adv. Funct. Mater.*, 2020, **30**, 1907962.
64 T. Duong, H. Pham, T. C. Kho, P. Phang, K. C. Fong, D. Yan, Y. Yin, J. Peng, M. A. Mahmud, S. Gharibzadeh, B. A. Nejand, I. M. Hossain, M. R. Khan, N. Mozaffari, Y. Wu, H. Shen, J. Zheng, H. Mai, W. Liang, C. Samundsett, M. Stocks, K. McIntosh, G. G. Andersson, U. Lemmer, B. S. Richards, U. W. Paetzold, A. Ho-Ballie, Y. Liu, D. Macdonald, A. Blakers, J. Wong-Leung, T. White, K. Weber and K. Catchpole, *Adv. Energy Mater.*, 2020, **10**, 1903553.
65 T. Zhu, D. Zheng, J. Liu, L. Coolen, T. Pauporté, T. Pauporte and T. Pauporté, *ACS Appl. Mater. Interfaces*, 2020, **12**, 37197–37207.
66 D. Luo, W. Yang, Z. Wang, A. Sadhanala, Q. Hu, R. Su, R. Shivanna, G. F. Trindade, J. F. Watts, Z. Xu, T. Liu, K. Chen, F. Ye, P. Wu, L. Zhao, J. Wu, Y. Tu, Y. Zhang, X. Yang, W. Zhang, R. H. Friend, Q. Gong, H. J. Snaith and R. Zhu, *Science*, 2018, **360**, 1442–1446.
67 K. Lee, J. Kim, H. Yu, J. W. Lee, C. M. Yoon, S. K. Kim and J. Jang, *J. Mater. Chem. A*, 2018, **6**, 24560–24568.
68 F. Zhang, Q. Huang, J. Song, Y. Zhang, C. Ding, F. Liu, D. Liu, X. Li, H. Yasuda, K. Yoshida, J. Qu, S. Hayase, T. Toyoda, T. Minemoto and Q. Shen, *Sol. RRL*, 2020, **4**, 1900243.
69 H. Dong, M. Yue, S. Pang, W. Zhu, D. Chen, H. Xi, Z. Lin, J. Chang, J. Zhang, Y. Hao and C. Zhang, *Sol. RRL*, 2019, **3**, 1900291.
70 C. Zhang, S. Wu, L. Tao, G. M. Arumugam, C. Liu, Z. Wang, S. Zhu, Y. Yang, J. Lin, X. Liu, R. E. I. Schropp and Y. Mai, *Adv. Energy Mater.*, 2020, **10**, 2002004.
71 S. Tan, I. Yavuz, M. H. Weber, T. Huang, C. Chen, R. Wang, H. Wang, J. H. Ko, S. Nuryyeva, J. Xue, Y. Zhao, K. Wei, J. Lee and Y. Yang, *Joule*, 2020, **4**, 2426–2442.
72 H. Kim, S. Lee, D. Y. Lee, M. J. Paik, H. Na, J. Lee and S. Il Seok, *Adv. Energy Mater.*, 2019, **9**, 1902740.
73 X. Zheng, B. Chen, J. Dai, Y. Fang, Y. Bai, Y. Lin, H. Wei, X. C. Zeng and J. Huang, *Nat. Energy*, 2017, **2**, 17102.
74 Q. Zhou, Y. Gao, C. Cai, Z. Zhang, J. Xu, Z. Yuan and P. Gao, *Angew. Chem.*, 2021, **133**, 8384–8393.
75 H. Wang, C. Zhu, L. Liu, S. Ma, P. Liu, J. Wu, C. Shi, Q. Du, Y. Hao, S. Xiang, H. Chen, P. Chen, Y. Bai, H. Zhou, Y. Li and Q. Chen, *Adv. Mater.*, 2019, **31**, 1904408.
76 T. M. Koh, V. Shanmugam, X. Guo, S. S. Lim, O. Filonik, E. M. Herzig, P. Müller-Buschbaum, V. Swamy, S. T. Chien, S. G. Mhaisalkar and N. Mathews, *J. Mater. Chem. A*, 2018, **6**, 2122–2128.
77 K. T. Cho, G. Grancini, Y. Lee, E. Oveisi, J. Ryu, O. Almora, M. Tschumi, P. A. Schouwink, G. Seo, S. Heo, J. Park, J. Jang, S. Paek, G. Garcia-Belmonte and M. K. Nazeeruddin, *Energy Environ. Sci.*, 2018, **11**, 952–959.
78 Y. Cho, A. M. Soufiani, J. S. Yun, J. Kim, D. S. Lee, J. Seidel, X. Deng, M. A. Green, S. Huang and A. W. Y. Ho-Baillie, *Adv. Energy Mater.*, 2018, **8**, 1703392.
79 P. Chen, Y. Bai, S. Wang, M. Lyu, J.-H. Yun and L. Wang, *Adv. Funct. Mater.*, 2018, **28**, 1706923.
80 Y. Lin, Y. Bai, Y. Fang, Z. Chen, S. Yang, X. Zheng, S. Tang, Y. Liu, J. Zhao and J. Huang, *J. Phys. Chem. Lett.*, 2018, **9**, 654–658.
81 M. Malekshahi Byranvand, F. Behboodi-Sadabad, A. Alrhman Eliwi, V. Trouillet, A. Welle, S. Ternes, I. M. Hossain, M. R. Khan, J. A. Schwenzer, A. Farooq, B. S. Richards, J. Lahann and U. W. Paetzold, *J. Mater. Chem. A*, 2020, **8**, 20122–20132.
82 J. Peng, D. Walter, Y. Ren, M. Tebyetekerwa, Y. Wu, T. Duong, Q. Lin, J. Li, T. Lu, M. A. Mahmud, O. L. C. Lem, S. Zhao, W. Liu, Y. Liu, H. Shen, L. Li, F. Kremer, H. T. Nguyen, D. Choi, K. J. Weber, K. R. Catchpole and T. P. White, *Science*, 2021, **371**, 390–395.

83 R. Wang, J. Xue, K.-L. L. Wang, Z.-K. K. Wang, Y. Luo, D. Fenning, G. Xu, S. Nuryyeva, T. Huang, Y. Zhao, J. L. Yang, J. Zhu, M. Wang, S. Tan, I. Yavuz, K. N. Houk and Y. Yang, *Science*, 2019, **366**, 1509–1513.
84 X. Liu, Z. Yu, T. Wang, K. L. Chiu, F. Lin, H. Gong, L. Ding and Y. Cheng, *Adv. Energy Mater.*, 2020, **10**, 2001958.
85 S. Yang, J. Dai, Z. Yu, Y. Shao, Y. Zhou, X. Xiao, X. C. Zeng and J. Huang, *J. Am. Chem. Soc.*, 2019, **141**, 5781–5787.
86 C. M. Wolff, L. Canil, C. Rehermann, N. Ngoc Linh, F. Zu, M. Ralaiarisoa, P. Caprioglio, L. Fiedler, M. Stolterfoht, S. Kogikoski, I. Bald, N. Koch, E. L. Unger, T. Dittrich, A. Abate and D. Neher, *ACS Nano*, 2020, **14**, 1445–1456.
87 Z. Liu, F. Cao, M. Wang, M. Wang and L. Li, *Angew. Chem.*, 2020, **132**, 4190–4196.
88 J. Xu, C. C. Boyd, Z. J. Yu, A. F. Palmstrom, D. J. Witter, B. W. Larson, R. M. France, J. Werner, S. P. Harvey, E. J. Wolf, W. Weigand, S. Manzoor, M. F. A. M. van Hest, J. J. Berry, J. M. Luther, Z. C. Holman and M. D. McGehee, *Science*, 2020, **367**, 1097–1104.
89 F. Peña-Camargo, P. Caprioglio, F. Zu, E. Gutierrez-Partida, C. M. Wolff, K. Brinkmann, S. Albrecht, T. Riedl, N. Koch, D. Neher and M. Stolterfoht, *ACS Energy Lett.*, 2020, **5**, 2728–2736.
90 S. Yang, S. Chen, E. Mosconi, Y. Fang, X. Xiao, C. Wang, Y. Zhou, Z. Yu, J. Zhao, Y. Gao, F. De Angelis and J. Huang, *Science*, 2019, **365**, 473–478.
91 F. Wang, Y. Zhang, M. Yang, D. Han, L. Yang, L. Fan, Y. Sui, Y. Sun, X. Liu, X. Meng and J. Yang, *Adv. Funct. Mater.*, 2021, **31**, 2008052.
92 P. Caprioglio, M. Stolterfoht, C. M. Wolff, T. Unold, B. Rech, S. Albrecht and D. Neher, *Adv. Energy Mater.*, 2019, **9**, 1901631.
93 J. Dagar, M. Fenske, A. Al-Ashouri, C. Schultz, B. Li, H. Köbler, R. Munir, G. Parmasivam, J. Li, I. Levine, A. Merdasa, L. Kegelmann, H. Näsström, J. A. Marquez, T. Unold, D. M. Többens, R. Schlatmann, B. Stegemann, A. Abate, S. Albrecht and E. Unger, *ACS Appl. Mater. Interfaces*, 2021, **13**, 13022–13033.
94 B. Park, N. Kedem, M. Kulbak, D. Y. Lee, W. S. Yang, N. J. Jeon, J. Seo, G. Kim, K. J. Kim, T. J. Shin, G. Hodes, D. Cahen and S. Il Seok, *Nat. Commun.*, 2018, **9**, 3301.
95 P. Fassl, V. Lami, A. Bausch, Z. Wang, M. T. Klug, H. J. Snaith and Y. Vaynzof, *Energy Environ. Sci.*, 2018, **11**, 3380–3391.
96 P. Fassl, Y. Zakharko, L. M. Falk, K. P. Goetz, F. Paulus, A. D. Taylor, J. Zaumseil and Y. Vaynzof, *J. Mater. Chem. C*, 2019, **7**, 5285–5292.
97 K. Wang, W. S. Subhani, Y. Wang, X. Zuo, H. Wang, L. Duan and S. (Frank) Liu, *Adv. Mater.*, 2019, **31**, 1902037.
98 D. Kim, H. J. Jung, I. J. Park, B. W. Larson, S. P. Dunfield, C. Xiao, J. Kim, J. Tong, P. Boonmongkolras, S. G. Ji, F. Zhang, S. R. Pae, M. Kim, S. B. Kang, V. Dravid, J. J. Berry, J. Y. Kim, K. Zhu, D. H. Kim and B. Shin, *Science*, 2020, **3433**, eaba3433.
99 D. S. Lee, J. S. Yun, J. Kim, A. M. Soufiani, S. Chen, Y. Cho, X. Deng, J. Seidel, S. Lim, S. Huang and A. W. Y. Ho-Baillie, *ACS Energy Lett.*, 2018, **3**, 647–654.
100 J.-W. Lee, Z. Dai, T.-H. Han, C. Choi, S.-Y. Chang, S.-J. Lee, N. De Marco, H. Zhao, P. Sun, Y. Huang and Y. Yang, *Nat. Commun.*, 2018, **9**, 3021.
101 M. Jung, T. J. Shin, J. Seo, G. Kim and S. Il Seok, *Energy Environ. Sci.*, 2018, **11**, 2188–2197.
102 Z. Wang, Q. Lin, F. P. Chmiel, N. Sakai, L. M. Herz and H. J. Snaith, *Nat. Energy*, 2017, **2**, 17135.
103 D. H. Kim, C. P. Muzzillo, J. Tong, A. F. Palmstrom, B. W. Larson, C. Choi, S. P. Harvey, S. Glynn, J. B. Whitaker, F. Zhang, Z. Li, H. Lu, M. F. A. M. van Hest, J. J. Berry, L. M. Mansfield, Y. Huang, Y. Yan and K. Zhu, *Joule*, 2019, **3**, 1734–1745.
104 C. Fei, M. Zhou, J. Ogle, D.-M. Smilgies, L. Whittaker-Brooks and H. Wang, *J. Mater. Chem. A*, 2019, **7**, 23739–23746.
105 N. Li, Z. Zhu, C. C. Chueh, H. Liu, B. Peng, A. Petrone, X. Li, L. Wang and A. K.-Y. Jen, *Adv. Energy Mater.*, 2017, **7**, 1–9.
106 S. Xiong, Z. Hou, S. Zou, X. Lu, J. Yang, T. Hao, Z. Zhou, J. Xu, Y. Zeng, W. Xiao, W. Dong, D. Li, X. Wang, Z. Hu, L. Sun, Y. Wu, X. Liu, L. Ding, Z. Sun, M. Fahlman and Q. Bao, *Joule*, 2021, **5**, 467–480.
107 X. Wang, K. Rakstys, K. Jack, H. Jin, J. Lai, H. Li, C. S. K. Ranasinghe, J. Saghaei, G. Zhang, P. L. Burn, I. R. Gentle and P. E. Shaw, *Nat. Commun.*, 2021, **12**, 52.
108 F. Zhang and K. Zhu, *Adv. Energy Mater.*, 2020, **10**, 1902579.
109 S. Liu, Y. Guan, Y. Sheng, Y. Hu, Y. Rong, A. Mei and H. Han, *Adv. Energy Mater.*, 2020, **10**, 1902492.
110 J. Wang, G. Jin, Q. Zhen, C. He and Y. Duan, *Adv. Mater. Interfaces*, 2021, **8**, 2002078.
111 X. Zhou, W. Qi, J. Li, J. Cheng, Y. Li, J. Luo, M. J. Ko, Y. Li, Y. Zhao and X. Zhang, *Sol. RRL*, 2020, **4**, 2000308.
112 D. Prochowicz, R. Runjhun, M. M. Tavakoli, P. Yadav, M. Saski, A. Q. Alanazi, D. J. Kubicki, Z. Kaszkur, S. M. Zakeeruddin, J. Lewiński and M. Grätzel, *Chem. Mater.*, 2019, **31**, 1620–1627.
113 L. Krückemeier, U. Rau, M. Stolterfoht and T. Kirchartz, *Adv. Energy Mater.*, 2020, **10**, 1902573.
114 L. Krückemeier, B. Krogmeier, Z. Liu, U. Rau and T. Kirchartz, *Adv. Energy Mater.*, 2021, **11**, 2003489.
115 Z. Liu, L. Krückemeier, B. Krogmeier, B. Klingebiel, J. A. Márquez, S. Levcenko, S. Öz, S. Mathur, U. Rau, T. Unold and T. Kirchartz, *ACS Energy Lett.*, 2019, **4**, 110–117.
116 B. Krogmeier, F. Staub, D. Grabowski, U. Rau and T. Kirchartz, *Sustainable Energy Fuels*, 2018, **2**, 1027–1034.
117 T. Kirchartz, J. A. Márquez, M. Stolterfoht and T. Unold, *Adv. Energy Mater.*, 2020, **10**, 1904134.
118 P. Fassl, V. Lami, F. J. Berger, L. M. Falk, J. Zaumseil, B. S. Richards, I. A. Howard, Y. Vaynzof and U. W. Paetzold, *Matter*, 2021, **4**, 1391–1412.
119 S. Zhang, S. M. Hosseini, R. Gunder, A. Petsiuk, P. Caprioglio, C. M. Wolff, S. Shoaee, P. Meredith, S. Schorr, T. Unold, P. L. Burn, D. Neher and M. Stolterfoht, *Adv. Mater.*, 2019, **31**, 1901090.
120 H. Jin, E. Debroye, M. Keshavarz, I. G. Scheblykin, M. B. J. Roeffaers, J. Hofkens and J. A. Steele, *Mater. Horizons*, 2020, **7**, 397–410.

121 W.-Q. Wu, P. N. Rudd, Z. Ni, C. H. Van Brackle, H. Wei, Q. Wang, B. R. Ecker, Y. Gao and J. Huang, *J. Am. Chem. Soc.*, 2020, **142**, 3989–3996.
122 P. Caprioglio, C. M. Wolff, O. J. Sandberg, A. Armin, B. Rech, S. Albrecht, D. Neher and M. Stolterfoht, *Adv. Energy Mater.*, 2020, **10**, 2000502.
123 N. E. Courtier, *Phys. Rev. Appl.*, 2020, **14**, 024031.
124 M. A. Green and A. W. Y. Ho-Baillie, *ACS Energy Lett.*, 2019, **4**, 1639–1644.
125 Z. Liu, J. Siekmann, B. Klingebiel, U. Rau and T. Kirchartz, *Adv. Energy Mater.*, 2021, 2003386.
126 H. Guthrey and J. Moseley, *Adv. Energy Mater.*, 2020, **10**, 1903840.
127 J. Hu, I. W. H. Oswald, S. J. Stuard, M. M. Nahid, N. Zhou, O. F. Williams, Z. Guo, L. Yan, H. Hu, Z. Chen, X. Xiao, Y. Lin, Z. Yang, J. Huang, A. M. Moran, H. Ade, J. R. Neilson and W. You, *Nat. Commun.*, 2019, **10**, 1276.
128 B. G. H. M. Groeneveld, S. Adjokatse, O. Nazarenko, H. Fang, G. R. Blake, G. Portale, H. Duim, G. H. ten Brink, M. V. Kovalenko and M. A. Loi, *Energy Technol.*, 2020, **8**, 1901041.
129 K. Du, Q. Tu, X. Zhang, Q. Han, J. Liu, S. Zauscher and D. B. Mitzi, *Inorg. Chem.*, 2017, **56**, 9291–9302.
130 K. Thirumal, W. K. Chong, W. Xie, R. Ganguly, S. K. Muduli, M. Sherburne, M. Asta, S. Mhaisalkar, T. C. Sum, H. Sen Soo and N. Mathews, *Chem. Mater.*, 2017, **29**, 3947–3953.
131 P. Cai, X. Wang, H. J. Seo and X. Yan, *Appl. Phys. Lett.*, 2018, **112**, 153901.
132 X. Chen, H. Lu, Z. Li, Y. Zhai, P. F. Ndione, J. J. Berry, K. Zhu, Y. Yang and M. C. Beard, *ACS Energy Lett.*, 2018, **3**, 2273–2279.
133 S. Béchu, M. Ralaiarisoa, A. Etcheberry and P. Schulz, *Adv. Energy Mater.*, 2020, **10**, 1904007.
134 R. D. Chavan, D. Prochowicz, P. Yadav, M. M. Tavakoli, A. Nimbalkar, S. P. Bhoite and C. K. Hong, *Sol. RRL*, 2019, **3**, 1900294.
135 T. Hellmann, C. Das, T. Abzieher, J. A. Schwenzer, M. Wussler, R. Dachauer, U. W. Paetzold, W. Jaegermann and T. Mayer, *Adv. Energy Mater.*, 2020, **10**, 2002129.
136 N. K. Noel, S. N. Habisreutinger, A. Pellaroque, F. Pulvirenti, B. Wenger, F. Zhang, Y.-H. Lin, O. G. Reid, J. Leisen, Y. Zhang, S. Barlow, S. R. Marder, A. Kahn, H. J. Snaith, C. B. Arnold and B. P. Rand, *Energy Environ. Sci.*, 2019, **12**, 3063–3073.
137 M. Caputo, N. Cefarin, A. Radivo, N. Demitri, L. Gigli, J. R. Plaisier, M. Panighel, G. Di Santo, S. Moretti, A. Giglia, M. Polentarutti, F. De Angelis, E. Mosconi, P. Umari, M. Tormen and A. Goldoni, *Sci. Rep.*, 2019, **9**, 15159.
138 B. Philippe, B. Park, R. Lindblad, J. Oscarsson, S. Ahmadi, E. M. J. Johansson and H. Rensmo, *Chem. Mater.*, 2015, **27**, 1720–1731.
139 A. A. Sutanto, P. Caprioglio, N. Drigo, Y. J. Hofstetter, I. Garcia-Benito, V. I. E. Queloz, D. Neher, M. K. Nazeeruddin, M. Stolterfoht, Y. Vaynzof and G. Grancini, *Chem*, 2021, **7**, 1903–1916.
140 S. Draguta, J. A. Christians, Y. V. Morozov, A. Mucunzi, J. S. Manser, P. V. Kamat, J. M. Luther and M. Kuno, *Energy Environ. Sci.*, 2018, **11**, 960–969.
141 J. Emara, T. Schnier, N. Pourdavoud, T. Riedl, K. Meerholz and S. Olthof, *Adv. Mater.*, 2016, **28**, 553–559.
142 Q. Wang, Q. Dong, T. Li, A. Gruverman and J. Huang, *Adv. Mater.*, 2016, **28**, 6734–6739.
143 H. Kanda, N. Shibayama, A. J. Huckaba, Y. Lee, S. Paek, N. Klipfel, C. Roldán-Carmona, V. I. E. Queloz, G. Grancini, Y. Zhang, M. Abuhelaiqa, K. T. Cho, M. Li, M. D. Mensi, S. Kinge and M. K. Nazeeruddin, *Energy Environ. Sci.*, 2020, **13**, 1222–1230.
144 A. Axt, I. M. Hermes, V. W. Bergmann, N. Tausendpfund and S. A. L. Weber, *Beilstein J. Nanotechnol.*, 2018, **9**, 1809–1819.
145 J. L. Garrett and J. N. Munday, *Nanotechnology*, 2016, **27**, 245705.
146 E. M. Lanzoni, T. Gallet, C. Spindler, O. Ramirez, C. K. Boumenou, S. Siebentritt and A. Redinger, *Nano Energy*, 2021, **88**, 106270.
147 D. H. Cao, C. C. Stoumpos, C. D. Malliakas, M. J. Katz, O. K. Farha, J. T. Hupp and M. G. Kanatzidis, *APL Mater.*, 2014, **2**, 091101.
148 R. A. Street, S. E. Ready, F. Lemmi, K. S. Shah, P. Bennett and Y. Dmitriyev, *J. Appl. Phys.*, 1999, **86**, 2660–2667.
149 Y. Sun, Z. Zhou, Z. Huang, J. Wu, L. Zhou, Y. Cheng, J. Liu, C. Zhu, M. Yu, P. Yu, W. Zhu, Y. Liu, J. Zhou, B. Liu, H. Xie, Y. Cao, H. Li, X. Wang, K. Liu, X. Wang, J. Wang, L. Wang and W. Huang, *Adv. Mater.*, 2019, **31**, 1806562.
150 Y.-M. Xie, X. Xu, C. Ma, M. Li, Y. Ma, C.-S. Lee and S.-W. Tsang, *ACS Appl. Mater. Interfaces*, 2019, **11**, 25909–25916.
151 S. Chen, X. Wen, J. S. Yun, S. Huang, M. Green, N. J. Jeon, W. S. Yang, J. H. Noh, J. Seo, S. Il Seok and A. Ho-Baillie, *ACS Appl. Mater. Interfaces*, 2017, **9**, 6072–6078.
152 S. I. Rahman, B. S. Lamsal, A. Gurung, A. H. Chowdhury, K. M. Reza, N. Ghimire, B. Bahrami, W. Luo, R. S. Bobba, J. Pokharel, A. Baniya, A. R. Laskar, K. Emshadi, M. T. Rahman and Q. Qiao, *ACS Appl. Mater. Interfaces*, 2020, **12**, 41312–41322.
153 T. Gallet, R. G. Poeira, E. M. Lanzoni, T. Abzieher, U. W. Paetzold and A. Redinger, *ACS Appl. Mater. Interfaces*, 2021, **13**, 2642–2653.
154 K. M. Reza, A. Gurung, B. Bahrami, A. H. Chowdhury, N. Ghimire, R. Pathak, S. I. Rahman, M. A. R. Laskar, K. Chen, R. S. Bobba, B. S. Lamsal, L. K. Biswas, Y. Zhou, B. Logue and Q. Qiao, *Sol. RRL*, 2021, **5**, 2000740.
155 D. Toth, B. Hailegnaw, F. Richheimer, F. A. Castro, F. Kienberger, M. C. Scharber, S. Wood and G. Gramse, *ACS Appl. Mater. Interfaces*, 2020, **12**, 48057–48066.
156 D. Kim, J.-H. Yun, M. Lyu, J. Kim, S. Lim, J. S. Yun, L. Wang and J. Seidel, *J. Phys. Chem. C*, 2019, **123**, 14144–14151.
157 T. Gallet, D. Grabowski, T. Kirchartz and A. Redinger, *Nanoscale*, 2019, **11**, 16828–16836.
158 J. Yang, S. Xiong, J. Song, H. Wu, Y. Zeng, L. Lu, K. Shen, T. Hao, Z. Ma, F. Liu, C. Duan, M. Fahlman and Q. Bao, *Adv. Energy Mater.*, 2020, **10**, 2000687.

159 C. Chen, Z. Song, C. Xiao, R. A. Awni, C. Yao, N. Shrestha, C. Li, S. S. Bista, Y. Zhang, L. Chen, R. J. Ellingson, C.-S. Jiang, M. Al-Jassim, G. Fang and Y. Yan, *ACS Energy Lett.*, 2020, **5**, 2560–2568.

160 S. Tan, I. Yavuz, N. De Marco, T. Huang, S. Lee, C. S. Choi, M. Wang, S. Nuryyeva, R. Wang, Y. Zhao, H. Wang, T. Han, B. Dunn, Y. Huang, J. Lee and Y. Yang, *Adv. Mater.*, 2020, **32**, 1906995.